Experimental Study On The Production Of Negative Ion Copper Clusters And Applications

A Thesis Presented for the

Master of Science

Degree

The University of Tennessee, Knoxville

Ran Chu

December 2016

For Ping Jiang, Deliang Chu and Ran Chu

Acknowledgements

I would like to take this opportunity to express my sincere gratitude to my advisor Professor Alfredo Galindo-Uribarri at Oak Ridge National Laboratories (ORNL) for providing me with the opportunity to pursue a higher education at University of Tennessee and ORNL. Without his help, this work would not be possible. Moreover, he patiently leads me into the academic world.

Thanks also to my thesis committee Dr.Anthony Mezzacappa and Dr. Thomas Papenbrock for their support and guidance.

I appreciate the entire team at the Holifield Radioactive Ion Beam Facility (HRIBF) for their assistance in my research, especially Dr.Yuan Liu for her invaluable suggestions and guidance and Gerald Mills for his help operating the stable ion beam injector negative ion source.

My sincere thanks also go to all members of UT Physics Department, especially Chrisanne Romeo, Marianne Breinig and Elisa Romero-Romero. They gave me suggestions and helped me all through my student life at UT and provided me with support through tough times.

Last but not the least, I would like to thank my family and friends. Thank you for your accompany.

What is this world?

Abstract

At the Holifield Radioactive Ion Beam Facility (HRIBF) at Oak Ridge National Laboratories (ORNL), we investigated the formation, production and potential application of negative-ion copper clusters using mass distributions of negative-ion copper clusters obtained by bombarding various copper samples with Cs ions. The Cu samples in very large mass-selected Cu clusters (e.g. size n=54) included natural Cu, isotopically enriched copper-63 and copper-65, and electroformed ultra-clean Cu. Mass spectra of negative copper clusters produced by a Cs sputter source with a size up to n = 50 are shown for the first time.

Three main features were observed for all four copper samples: the intensity of the copper cluster ions exhibits an even-odd alternation because of electron pairing in the highest occupied molecular orbitals; a discontinuity in the ion intensity at magic numbers n = 2, 8, 20, 40 due to the close of a shell in the shell model; the abundance of a copper cluster has a power-law dependence on its size n. The exponent we measured for the copper cluster was ~ 3.

In addition, by having access to various samples of copper, including isotopically enriched material, we were able to study the formation of clusters involving various combinations of copper-63 and copper-65. A binomial distribution was observed for the formation of Cu clusters from natural Cu and clean Cu samples and it indicates that the formation of a sputtered copper cluster is a random multiple sequential aggregation. We show for the first time that the isotopes exhibit a binomial distribution in a metal cluster.

We explored a potential application of copper clusters, utilizing the energy-and-mass-selected copper cluster to prepare nanoporous graphene for applications such as water desalination. Copper clusters of size (n = 3 and 9) and energy 200 keV were applied to bombard the single-layer graphene with various dosages. Raman spectrum and scanning electron microscopy showed diameter around 2 nm defects were created.

Table of Contents

List of Tables

List of Figures

Chapter 1

Introduction and Motivation

Metal clusters are aggregates of metal atoms with well-defined size varying from several to tens of thousands. They are finite fermion systems and the delocalized valence electrons provide the bonding for the metal clusters, which makes the quantum properties of metal clusters determined by the finite system of delocalized electrons and to have a nuclei-like shell structure.

The study of metal clusters is important for several reasons:

First, cluster physics constitutes a field that lies between atomic and molecular physics on the one hand and condensed matter physics on the other hand. It is the paradigm for understanding how matter builds up from its elementary constituents. Metal clusters provide a relatively simpler tool for studying the properties of finite fermion systems with increasing sizes from atomic microscopic dimensions all the way to the macroscopic domain.

Second, the study of clusters constitutes an interdisciplinary field nature where both physics and chemistry questions need to be addressed.

Third, atomic metal clusters are also interesting for nuclear physics [16], especially after the discoveries of electronic shell structures and supershell structure in small alkali metal clusters. Researchers have discovered that many interesting similarities exist between cluster physics and nuclear physics: the basic model of the nucleus is

the shell model where the nucleons move in a common self-consistent field and interact through residual interactions while the simplest model of alkali metal clusters is the "jellium model" where the electrons move in a static potential due to the positive ions and interact through their Coulomb interactions [6]. Neutral clusters have practically no limit to their sizes, unlike nuclei whose size is limited by the Coulomb repulsion between protons to mass numbers $A = N + Z \leq 300$. Some of the cluster theories can be applied to provide confirmation for some theoretical predictions of nuclei, such as fermionic supershell, which could never be confirmed in nuclei because the size of the oscillation period is large. In some ways, simple metal clusters allow for "clean" studies of the dynamics of finite fermion systems.

Moreover, as observed, metal clusters change their physical properties spontaneously from a distinct size: metal particles below about 2 nm show typical quantum size behavior even at room temperatures owing to the existence of discrete electronic energy levels and the loss of overlapping electronic bands, the characteristic of a bulk metal. Some other properties changes on the way from bulk to molecule or vice versa besides the exciting electronic changes: small metal clusters show a significantly lower melting point than that of the corresponding bulk metal; the magnetic and optical properties of clusters, and the band gap of semiconductor clusters, all show a dependence on the cluster size[44]. Therefore, metal clusters are considered as links between bulk metals and small molecular clusters.

In principle, metal clusters have two different procedures for their generation: bottom up and top down. Bottom-up strategies use single atoms or ions to grow clusters while top-down syntheses start from bulk metal and apply techniques that destroy the bulk structure[44]. The procedure used in our experiments was a bottom-up strategy – cluster formation from sputtered species. More details about the formation and the behaviors of the copper clusters and their theoretical explanation of their formation process can be found in Chapter 2 and Chapter 4.

1.1 Copper clusters

The present study focuses on the production and characterization of copper clusters. Our interest in the study of copper clusters derives not only from the fundamental importance of cluster physics but also from the practical applications of copper cluster ion beams. Our interest on copper derived from a specific application to develop ultra-sensitive analytical techniques for the MAJORANA project. The MAJORANA project is an experiment designed to search for neutrinoless double-beta decay using highly-enriched germanium-76 as a source and a detector. The identification of the neutrino as a Majorana particle could be revealed from the observation of neutrinoless double-beta decay. The initial phase of the MAJORANA experiment is the Majorana demonstrator project (MJD) which is aimed to demonstrate a detector of 40 kg enriched ^{76}Ge with sufficiently low background. Current experimental results[38] indicates that the half-life of neutrinoless double beta decay of ^{76}Ge is larger than 2.1×10^{25}yr, which sets a limit on the required background to one count per tonne-year in the narrow region of interest around the expected ^{76}Ge neutrinoless double-beta decay peak[40]. In order to achieve such low backgrounds, the MJD detector is constructed and operated at 4850' below the earth surface in the Sanford Underground Laboratory in Lead, South Dakota to avoid the background from cosmic rays. In addition, due to this extreme requirement on the background, the purity of the construction materials is unprecedented: impurities can be a source of background and must be kept extremely low. For example, Monte Carlo simulations indicate that uranium (^{238}U) and thorium (^{232}Th) impurities in the copper used are expected to be the dominant sources of background and must be below the levels of a few 10^{-14} by weight. Consequently, the detector mounts and cryostat are made made from ultra-pure copper electroformed and machined in the underground laboratory. Therefore, it is necessary to verify that the impurities in the ultra-pure copper are sufficiently low.

Accelerator Mass Spectrometry (AMS)[51] has been proposed to evaluate the impurities in the ultra-pure copper materials for MJD. In particular, we are concentrated on determining U and Th in the copper[42]. AMS is an ultra-sensitive technique capable of single atom counting. However, to achieve single atom counting, optimization of the mass spectrometry and the detector is very important. In in order to detect the ultra-trace-level U and Th by AMS, copper cluster beams are injected to tune the AMS. Detail discussion can be found in Chapter 3.

An important application of copper clusters is the production of nanoporous single-layer graphene by cluster ion beam etching. This application has been studied in the present work and will be described in Chapter 5.

1.2 Mass spectrometry and copper cluster studies

A number of techniques have been used in the study of copper clusters, including time-of-flight photoelectron spectroscopy [7, 25, 34, 39]; sector-type mass spectrometry[27]; time-of -flight mass spectrometry[14, 43, 57]; and laser photodetachment [59]. For those studies, three types of cluster beam sources have been reported [20]: supersonic cluster beams[15, 59], inert gas condensation sources (including laser vaporization cluster source) [17, 36, 43] and sputtering cluster sources[14, 17, 25, 57].

In the present study, a cesium-sputter negative ion source is used to produce negatively charged copper cluster ions. A sputter source is efficient in producing large cluster ions. For example, with a 10 keV Xe sputter source with primary current both about 7 μA, Katakuse et al. produced positive copper clusters ions up to a cluster size of $n = 150$ and resolved peaks up to $n = 70$[27] and negative copper cluster ions up to cluster size $n = 80$[28]. In our experiments, the intensity of the primary Cs beam can be up to 0.1 mA.

The rest of this dissertation is organized as follows. Chapter 2 gives an introduction to the theoretical aspects of copper cluster production. Chapter 3 describe the experimental setup for our experiments. Chapter 4 presents the

experimental results and the analyses of the observed characteristics of copper clusters, including the even-odd alternation, magic numbers, power law dependence, and binomial distributions. Chapter 5 presents the investigation on the application of copper clusters in the production of nanoporous graphene, including the experimental setup and the results are discussed. In Chapter 6, we summarize our results and give an outlook for future research.

Chapter 2

Theory

The copper clusters in our experiments are produced in a cesium sputtering ion source. More precisely, copper clusters are emitted from the bulk copper surface under the bombardment of positive Cs ions. The research field of sputtering is rather broad and it is beyond the scope of this thesis. This chapter provides an introduction to sputtering theories rather than a review and introduces the concepts such as sputter yield and power law dependence in cluster formation.

2.1 Description of the sputtering process

Figure 2.1 illustrates the sputtering process and secondary-ion emission. The primary Cs^+ beam hits the sample surface and transfers sufficient energy to the surface particles so that they can overcome the surface binding energy. Atomic and molecular fragments will be sputtered from the sample surface, escaping to the vacuum. The main components of these sputtering beam are neutral atoms and clusters. During this process, some of the secondary particles emitted will be ionized. Charged particles, including both positive and negative charged particles, only constitute a fraction, between 10^{-3} to 10^{-4}[3]. The emission of negative ions from metal surfaces bombarded by positive cesium ions was first observed in 1962[32]. About ten years after the discovery, in 1973, Herzog, Poschenrieder and Satkiewicz published[23]

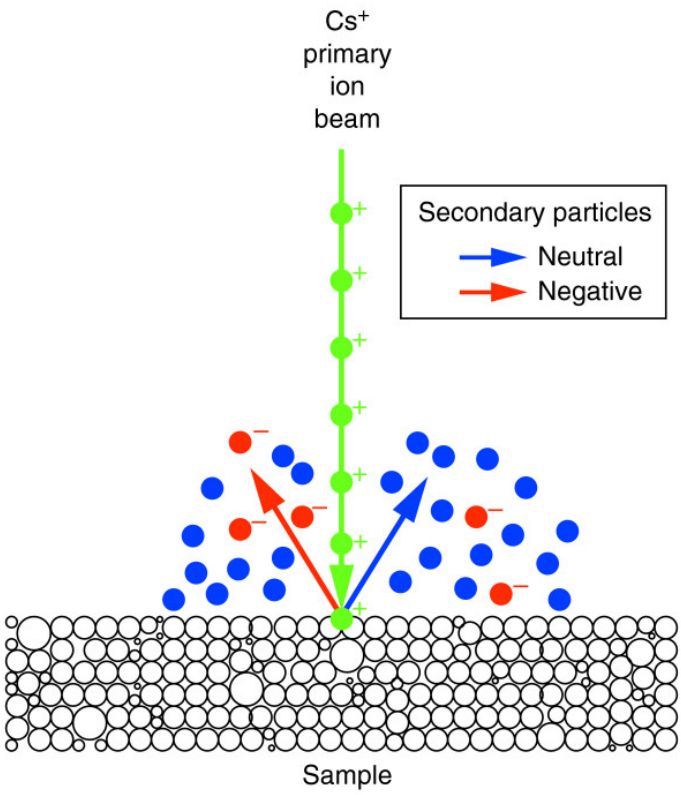

Figure 2.1: Principle of secondary-ion emission under Cs^+ ion sputtering. Adapted from [33].

their results they obtained in 1966, about the observation of clusters emitted from metallic surface (Al, Si and Mg) using a He^+, Ar^+ and Xe^+ sputtering ion source with bombarding energies between 4 to 12 keV. Since then, metal cluster production by sputtering was heavily investigated. In 1973, Sigmund[46] proposed a model to explain the mechanism of surface micro-roughening by ion bombardment. In his description, an impinging primary ion experiences a series of linear collisions in the target material, recoiling atoms with sufficient energy go through secondary collisions and create further generations of recoiling atoms. Some of the recoiling atoms gain sufficient energies to overcome the surface binding and leave the target surface as secondary ions. Sigmund believed that the majority of sputtered particles emitted from clouds of high order recoil atoms has very low energies (several electron volts) and originate from the uppermost atomic layers of the target.

2.1.1 Collision cascade regimes

There are three possible collision cascade regimes and they can be distinguished by the energy of the recoiling target atoms and the spatial density of the recoils[19]. The three collision cascade regimes are single knock-on regime, the linear-cascade regime, and collision spike (nonlinear cascade) regime.

Single knock-on regime is expected if the target is bombarded with low energy or by a light projectile, such as H and He. Only small energy is transferred to the target atoms which is not enough to generate recoil cascades and only a few collisions can occur (Figure 2.2a). In this case, the collision happens near the surface.

Linear-cascade regime will be considered if the target is bombarded under energies exceeding a few hundred eV by medium or high masses. Large energy is transferred to the target atoms and leads to the evolution of larger collision cascades. (Figure 2.2b) The collisions are assumed to happen between a moving atom and a rest atom and deeper than where the collisions of single knock-on regime happen. It is so-called linear because the solving of the Boltzmann transport equation describing the collision cascade is linearized. In this case, the sputtering yield was predicted to scale linearly with the energy deposited in elastic collisions as the target surface[45, 48].

If the projectile consists of heavy masses having a high energy up to 10keV, a *collision spike regime* applies. Huge energy is transferred to the target atoms and the majority of atoms within the cascade volume are in motion, instead of a small fraction of atoms in a linear cascade(Figure 2.2c). As a consequence, the sputter yield rises super-linearly (nonlinear) with the energy deposited at the target surface. More specifically, the sputter yield varies more rapidly than proportional to the square of deposited energy[19, 48].

2.1.2 Sputtering yield

During the sputtering process, materials are sputtered from the target surface. The erosion of this sputtering process is measured by the sputtering yield Y which is

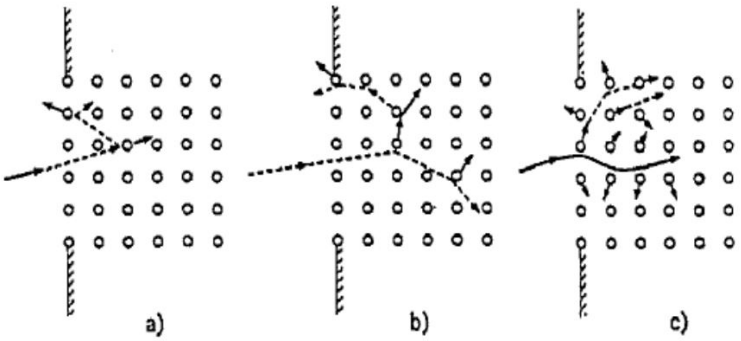

Figure 2.2: A schematic representation of the sputtering process by elastic collisions: (a) the single knock-on regime; (b) the linear cascade regime; (c) the spike regime in which there is a high density of recoil atoms so that most atoms in a certain volume are moving. Adapted from [19].

defined as the mean number of atoms removed from the surface of a solid per incident particle. Sigmund[45] proposed a general yield expression:

$$Y(E) = \Lambda K N S_n(E), \tag{2.1}$$

where Λ is a material constant, K is a dimensionless correction factor, N is the atomic density of the target, and $Sn(E)$ is the nuclear stopping cross section as a function of the initial energy E of the projectile.

The $Y(E)$ have a different form for low and high sputter energy. For ion energies smaller than 1keV, the yield[46] is

$$Y(E) = \frac{3}{4\pi^2} K \frac{\gamma E}{U_o}, \tag{2.2}$$

where γ is the energy transfer mass factor for elastic collisions:

$$\gamma = \frac{4M_1M_2}{(M_1 + M_2)}, \tag{2.3}$$

and U_0 is the surface binding energy (the minimum energy needed to remove an atom from the surface).

For energies greater than 1keV, the yield[46] can be parametrized as

$$Y(E) = \frac{(0.042\mathring{A}^{-2})KS_n(E)}{U_0}. \tag{2.4}$$

For elastic collisions with projectile ion with atomic number Z_1 and atomic mass M_1 moving with velocity v collides with an target having atomic number Z_2 and atomic mass M_2,

$$S_n = \frac{\pi^2 Z_1 Z_2 e^2 a M_1}{2(M_1 + M_2)}, \tag{2.5}$$

$$S_n(E) = \frac{1}{1-m} C_m \gamma^{1-m} E^{1-2m}, \tag{2.6}$$

where C_m is constant. For low energy (m $\approx$ 0), the $S_n(E)$ increase linearly with E. For high energy (m $\approx$ 1), the $S_n(E)$ falls and decrease like E^{-1} and diverges due to the $\frac{1}{1-m}$ factor. The change point is $m = 0.5$.

2.2 Theoretical models of formation of sputtered cluster

To gain a better understanding of the mechanisms of the formation of clusters during the sputtering process and reproduce experimental quantities, some theoretical models were proposed, such as direct emission mechanism (DEM), atomic combination mechanism (ACM), thermodynamic model, shock wave model, etc. The following paragraphs briefly outline the most important of them.

Direct emission mechanism assumes that one single collision takes place between a recoil atom from the collision cascade in the target and a molecule already present at the target surface and these two leave the surface as a molecule. DEM requires the relative kinetic energy E_{cm} in the center-of-mass-system of the atom low enough to prevent fragmentation but large enough to overcome the binding force between the molecule and the surface. That is, E_{cm} must be lower than the dissociation energy D

but larger than the binding energy U_0 of the molecule. Since in metals the dissociation energy D of a dimer is typically smaller than the surface binding energy U_0, the above requirement is unlikely to be met; that is, the emission probability of an intact dimer is practically zero in experiments[2, 19].

If the dimers are not formed by two atoms combination, another possibility is that dimers are formed from independently ejected atoms. *The atomic combination mechanism* (ACM) follows this idea and proposes that dimers or larger clusters are formed from independently ejected atoms, when they are emitted with close time-space position and their relative kinetic energies are less than the binding energy of the corresponding clusters. It has been shown[56] that the ACM model predicts an exponential yield decay with increasing cluster size rather than the power law dependence widely observed. Therefore, although ACM is successful in describing the yields of sputtered metal dimers and trimers[18], it fails for large clusters.

Urbassek[52] made an assumption that after the high energy bombardment, small clusters are emitted from the surface near regions of the target, the energized cascade volume begin to equilibrate thermally. Computer simulation results implied that thermalization may occur of the target surface after bombarded with energetic ions and this fact inspired *the thermodynamic model*. Thermalization the target surface leads to the vaporization of part of the irradiated material, with concomitant strong cluster abundance. In this case, the predicted cluster size distribution depends on the average initial energy density: a small number of atoms evaporate for a small initial energy density; a polynomial decay of the abundance distribution for the intermediate initial energy density; an exponential cluster distribution of the abundance distribution for the high initial energy density. This model was discussed in the light of the critical point of the gas-liquid phase transition and it predicts that cluster mass distribution can obey a power law with an exponent of 7/3 or a combination of the two. This model was successfully applied[10, 52] to fit mass distributions of Ar_n^+,N_n^+,Ni_n^+ and $[Cs(CsI)_n]^+$.

Shock wave model[5] is proposed to describe the formation of $n > 3$ clusters emitted when a high energy heavy ion interact with a solid surface. Both experimental and theoretical results[47]have shown that the clusters are formed with the greatest probability under heavy ion bombardment. This leads to a drastic increase of the sputtering yields due to the overlapping of elastic collision cascades. The overlap of the collision cascades and the formation of a high-density energy deposition region could be the source of a shock wave[5]. In fact, this model succeeds to predict a power law dependence of cluster yields, but it does not give the dependence of the exponent on bombardment conditions. The calculated values of exponent ~ 2 are not in agreement with the experimental data (where the exponent is in the range of 4 to 8)for metal sputtering[14, 56]. Recently, Rehn et al[41] and Staudt[49] reported the experimental observations that the formation of large sputtered clusters up to $n > 500$ atoms (Rehn) or $n > 50$ (Staudt) may obey the shock wave model with an exponent α of 2.

2.2.1 Power law dependence

Numerous studies have been devoted to investigate sputtered clusters at different bombarding conditions. In particular, metallic samples as model systems for purely collisional sputtering conditions has been widely studied. It has been observed that for both ionic and neutral clusters, the yields of different clusters exhibit a power law dependence on the cluster size n:

$$Y \propto n^{-\alpha}. \tag{2.7}$$

Exponent α is a constant and is found to be related to the total sputter yield which strongly depends on the bombarded material[12, 56] as well as on the bombarding conditions such as bombarding energy and primary ion species [13, 57]. A wide range of α values for various metal clusters have been reported in the literature, ranging from around 3 [29] to larger than 10 [29]. In particular, α values of 6-8 have been

Table 2.1: Summary of the exponent of power law dependence on cluster size

Element	Exponent
Al	7.7 and 8.6[56] 9.3 [12]
Cu	3.82[29] 7.8 [12] 8.1, 8.2 and 6.2 [13]
Nb	8.1[56]
Ag	5.3 and 6.0[56] 6.5[57]
In	2.1[49] 4.1[35] 5.6[35]
Ta	8.5[56]
Au	2.8[29]

reported[10, 13] for Cu clusters produced in the sputter of polycrystalline copper surfaces by Ne^+, Ar^+ and Xe^+ ions.

The power law dependence of the cluster yields on the cluster size is a general phenomenon and has been reported in many cluster experiments(Al_n [12, 56], Cu_n [12, 13, 29], In_n [35, 49], Ag_n [56, 57], Ta_n [1, 56], and Nb_n [56]). As summarized in Table 2.1, the previous experiments show that the exponent of small clusters (size $n \leq 40$) ranges between 2 and 9. For copper clusters, the largest α observed by Coon et al. is 8.2[13], while the smallest exponent of 3.82 is measured by King et al. [29].

So far there are no simple theoretical models that can predict both the power law dependence of the cluster distributions and the experimentally observed high values of the exponent α. Two models that can give a power law distribution are the shock wave model of Bitensky and Parilis[5], which predicts a value of around 2, and the thermodynamic equilibrium model of Urbassek[52] that gives a α value of around 7/3. It is therefore interesting to study the power law dependence of the negative copper clusters produced in the present experiment.

2.3 Negatively charged clusters

The copper clusters obtained in this study are negatively charged cluster ions produced in a cesium sputter ion source. As discussed previously, during the sputtering process a fraction of the secondary particles are ionized. The probability of secondary negative ion emission can be quantitatively described by a modified Saha-Langmuir equation[32]:

$$\alpha^- = \frac{\omega^-}{\omega^0 e^{(EA-\phi)/kT}} \tag{2.8}$$

where α^- is the ratio of negative ions to neutrals, EA is the electron affinity, ϕ is the effective work function of the sputter surface, T is a temperature parameter whose magnitude is greater than the true temperature of the surface, and the ω^- and ω^0 are the partition function. This equation indicates that for efficient negative ion production, the difference $(EA - \phi)$ should be as small as possible. This can be affected by two means: higher electron affinity and lower surface work function. For a fixed work function, higher negative ion yields are expected for clusters with higher electron affinities. Since the EA values cannot be changed, the possible enhancement will come from lowering the work function.

Electron affinity (EA) is defined as the amount of energy released or spent when an electron is added to a neutral particle to form a negative ion. A positive EA indicates energy released when gaining the extra electron while a negative EA indicates energy spent. Thus, a positive EA indicates that the resulting negative ion is stable. A particle has a more positive EA value is more likely to accept an electron and is so-called an electron acceptor. Figure 2.3 shows the electron affinity of copper clusters as a function of cluster size n. As we can see, the EAs of certain cluster sizes, such as n = 8, 14, 20, 30, 34, and 40, are noticeably smaller than the neighboring clusters. Therefore, relative lower negative cluster yields are expected for these clusters. They correspond to the so-called magic numbers which will be discussed in Chapter 4.

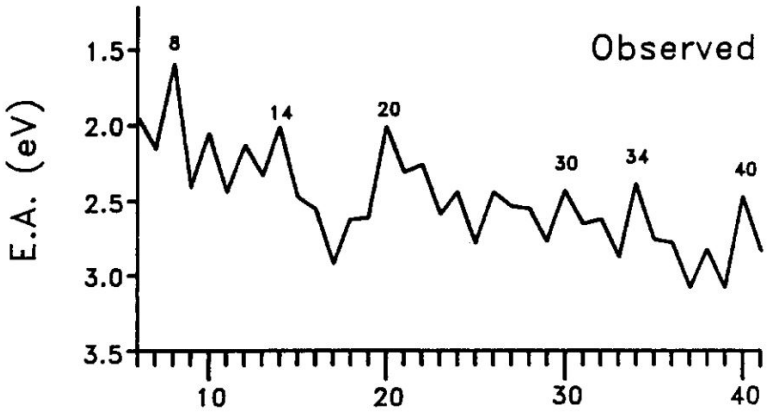

Figure 2.3: Measured (vertical) electron affinity of copper clusters. Adopted from [39]

2.3.1 Cs layer and the work function

Work function is the minimum thermodynamic work (energy) needed to remove an electron from a solid to a point in the vacuum immediately outside the solid surface. It is a property of the surface of the material. The work function of Cs elements is 2.1 eV[21]. It is well known that the addition of sub-monolayer of alkali atoms such as cesium to the surface can considerably reduce the work function and enhance the probability of negative ion production[30, 32]. In fact, the cesium in the Cs-sputter negative ion source has two functions: (1) to provide projectile ions to bombard the surface and (2) to lower the work function of the sputter side to increase the negative ion yield. More details of the Cs-sputter ion source will be given in the next Chapter.

Chapter 3

Experimental Setup

3.1 Mass spectrometry layout

The experimental setup used in this study is the first stage of the Accelerator Mass Spectrometry (AMS) system based on the 25-MV tandem accelerator at the Oak Ridge National Laboratory (ORNL). AMS is an ultra-sensitive technique for isotopic analysis. It is used to measure isotopic ratios for specific elements to a level of 1 in 10^{15}[51]. AMS is used to detect concentrations of natural isotopic abundances of both radionuclides and stable nuclides. AMS has been widely applied in many fields, such as archeology, geology, oceanography, biomedicine, environmental studies, and nanomaterials[22]. Comparing to conventional radiometric methods, the main advantages of AMS include a high degree suppression of isotopic and isobaric contaminants, high sensitivity, smaller sample quantities (mg and even sub-mg size), and shorter measuring times.

Figure 3.1 is a schematic view of the 25-MV tandem accelerator facility at ORNL. A beam of negative ions is formed with a negative Cs sputtering ion source (A) and accelerated in the injector acceleration tube (B) bringing its energy to typically between 150-300 keV. The beam is mass analyzed by a 90-degree dipole magnet analyzer (C) which bends the beam of selected mass vertically into the tandem.

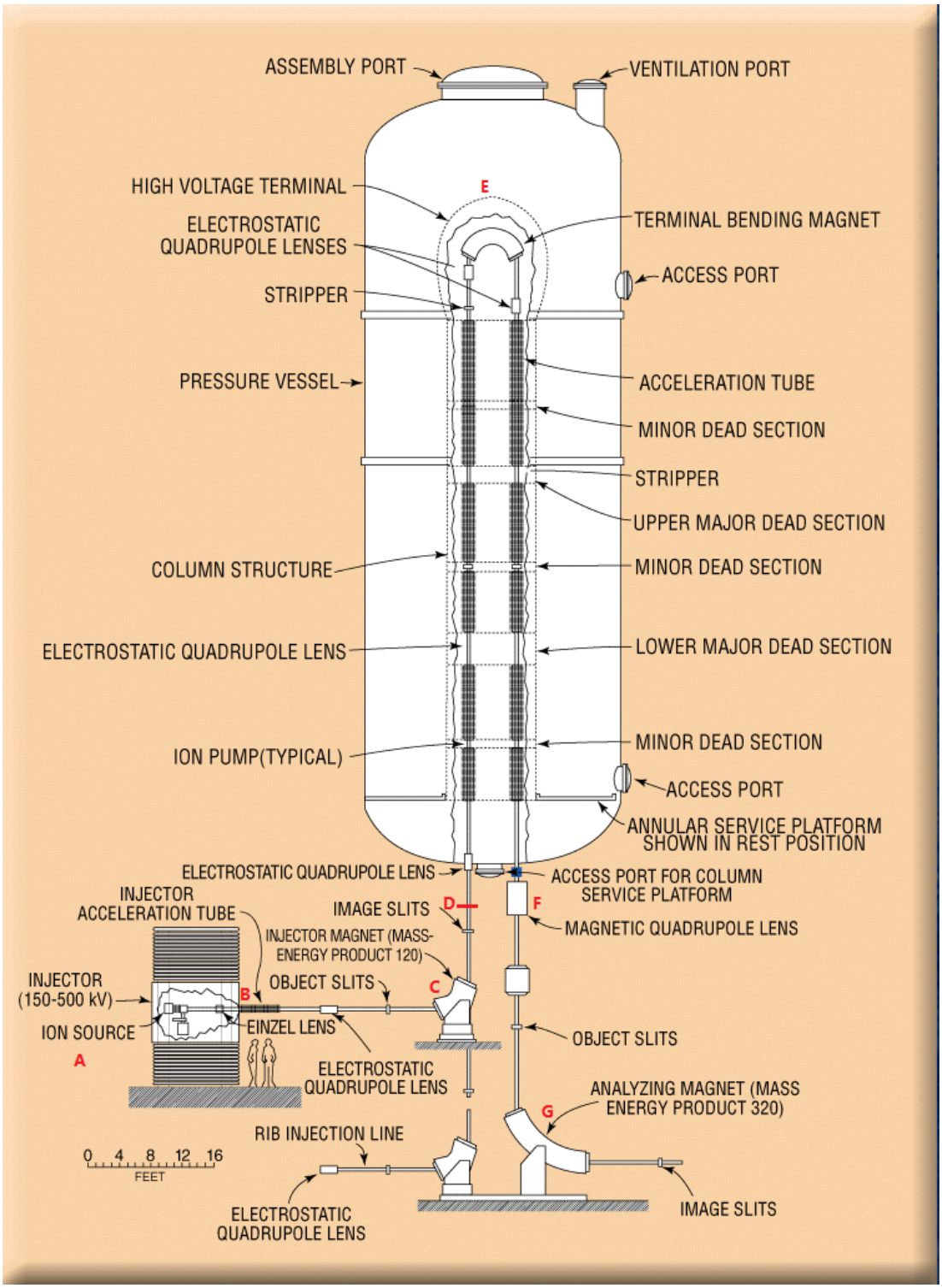

Figure 3.1: A schematic view of the 25-MV tandem accelerator.

The 25-MV tandem is a vertical tandem electrostatic accelerator with a folded configuration. Negative ions are required as the input ions which are accelerated up towards the positively charged terminal. Near the terminal the negative ions pass through a foil or gas stripper and after electron removal they become positively charged ions. The resulting positive ions of a charge state of interest are selected by the 180-degree terminal bending magnet (E) and then accelerated down the high-energy side of the tandem. After the tandem, the high-energy positive ion beam is further mass-selected by another analyzing magnet (G) before being sent to the experiments. For this study, the negative ions were not injected into the tandem. Instead, we gathered the beam and analyzed its intensity behind the image slits (D) with a Faraday cup as sketched in Figure 3.1.

3.2 Cs sputter negative ion source

Negative ions are required for injection into the 25-MV tandem electrostatic accelerator. The negative ion source at HRIBF is a single cathode Cs-sputter negative ion, usually called the Source of Negative Ions by Cesium Sputtering (SNICS) from National Electrostatics Corporation (NEC). A schematic drawing of the SNICS is given in Figure 3.2.

The negative ion source operating principle is illustrated in Figure 3.4. It has a conical geometry, W-surface ionizer that is heated to high temperatures higher than 1000^{o}C for surface ionization of Cs atoms. The sputter cathode (Cu target in Figure 3.2) is attached to a water-cooled rod. Cesium vapor from a heated external Cs oven is introduced into the enclosed area between the cooled cathode and the heated ionizer. (Figure 3.3) Some of the Cs vapor hits the hot ionizer, and the Cs atoms are thermally ionized on the ionizer surface. Then the positive Cs ions are accelerated towards and focused on the cathode by the electric field between the W-ionizer and the cathode that is maintained at a negative voltage of a few kV relative to the ionizer. Neutral species and ions, are sputtered from the sample surface by the

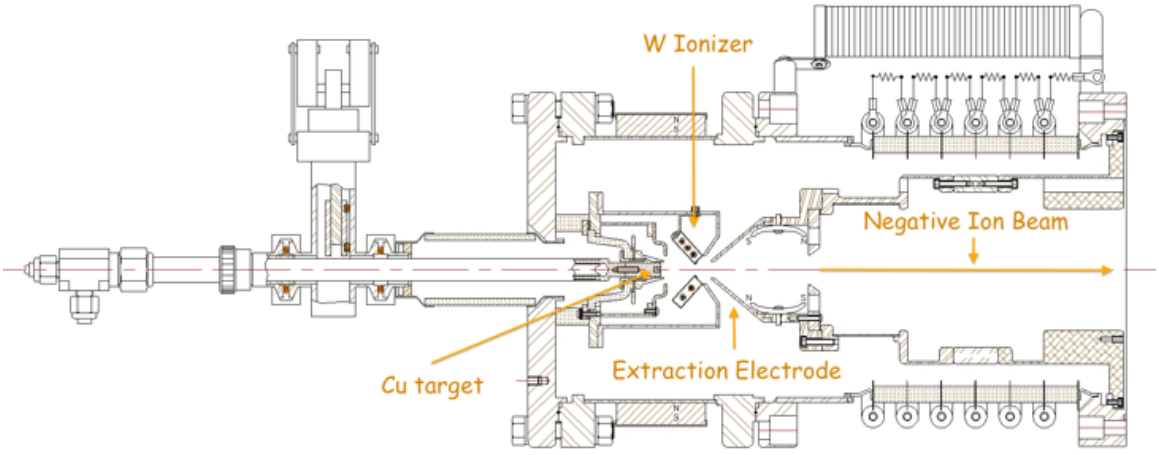

Figure 3.2: A schematic drawing of the cesium beam sputter source which we applied.

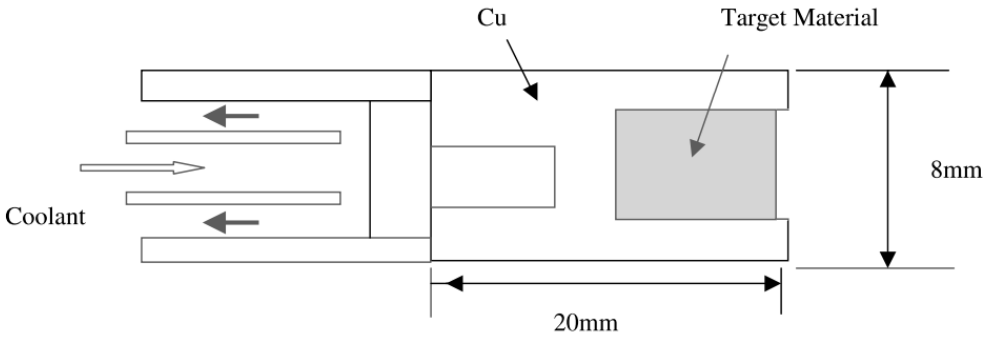

Figure 3.3: Schematic drawing of the sputter cathode for SNICS.

energetic Cs^+ ions.(Figure 3.4) A fraction of the sputtered species leaves the surface as negatively charged ions which are extracted and accelerated away from the sample surface by the same ion optics that accelerates Cs^+ ions. A beam of negative ions is then obtained. As discussed in the previous chapter, the probability of negative ion formation depends on the electron affinity of the species and the work function of the cathode surface. In general, lower surface work function leads to higher yields of negative ions. Some of the Cs vapor condenses on the sample and forms a thin surface layer that considerably reduces the surface work function and significantly enhances the probability of negative ion production[30].

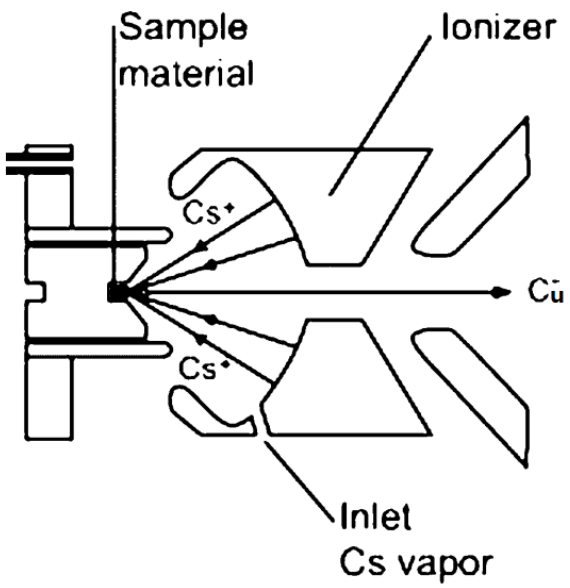

Figure 3.4: Operating principle of the Cs-sputter negative ion source.

Figure 3.5a shows a photo of the SNICS ion source mounted on the ion source platform that is maintained at a negative high voltage. Negative ions extracted from the ion source are accelerated into the injection beamline that is at ground potential. Thus, the ion beam energy is determined by the bias voltage of the ion source platform. Typically, the ion source platform is biased at 200 kV. Figure 3.5b shows another photo of the SNICS source, which shows the cathode rod being pulled out of the ion source.

3.3 Mass analysis system

After the Cs-sputter ion source, ion beams are accelerated into a 90 degree dipole magnet which separates ions according to their mass-to-charge ratio. In the dipole magnet, a uniform magnetic field is applied in the direction perpendicular to the direction of the ion motion, which applies a Lorenz force to the ions:

$$\vec{F} = q\vec{v} \times \vec{B}, \tag{3.1}$$

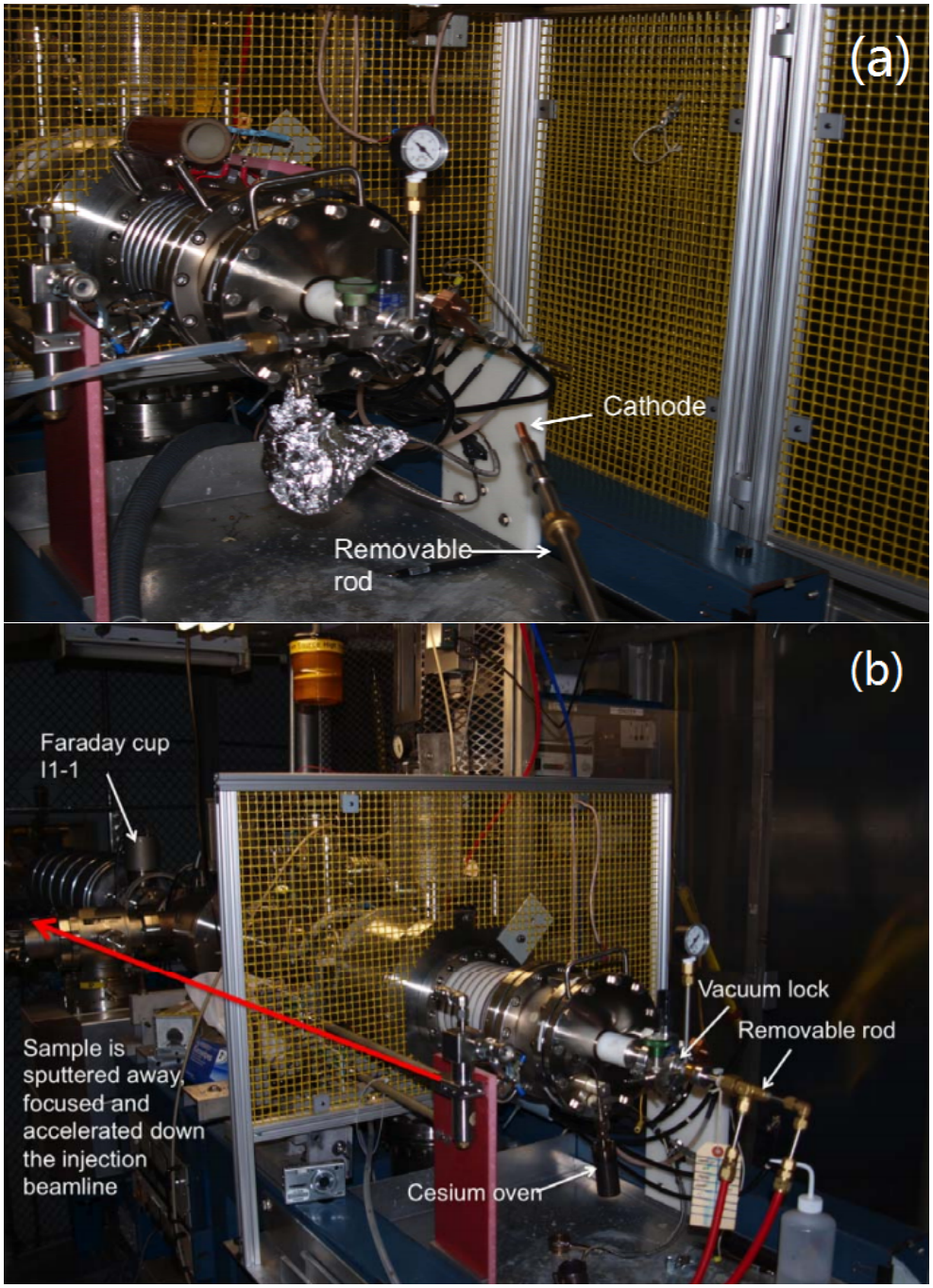

Figure 3.5: (a) the single cathode SNICS mounted on the high voltage platform. The cathode containing the target material is screwed onto the end of a removable rod and is inserted into the focal point of the SNICS through a vacuum lock. (b) a photo of the SNICS with the sample rod pulled out of the source. Cesium vapor is supplied from an external Cesium oven as shown in the photo. The Faraday cup 11-1 measures the total ion beam current from the ion source. Adapted from [24].

where q is the charge of the ions, $\vec{v}$ is the ion velocity, and $\vec{B}$ is the magnetic field. As a result, the ions travel in a circular path in the plane of motion. Only the ions that have equal centripetal and Lorenz forces can pass through the image slit (D in Figure 3.1) of the dipole magnet:

$$M \cdot \frac{v^2}{R} = qvB, \tag{3.2}$$

where R is the radius of the circular path curvature. The kinetic energy E of the ions is given by

$$E = qV = \frac{1}{2}Mv^2, \tag{3.3}$$

where V is the acceleration voltage. Substituting for v using Equation 3.3, one obtains

$$BR = \frac{Mv}{q} = \frac{\sqrt{2ME}}{q}, \tag{3.4}$$

which can be rewritten as

$$2(\frac{M}{q})(\frac{E}{q}) = (BR)^2. \tag{3.5}$$

The parameter BR is referred to as the "magnetic rigidity", which represents the required magnetic bending strength for a given ion radius and energy. In the experiments, R is the radius of the magnet which is fixed to be certain constant, E is set to a preferred value, and we select ions by adjusting the B.

The 90 degree magnet used for this study has R = 1 m and the maximum magnetic field B_{max} = 1.8 T. Therefore, the maximum ion mass that can pass through the magnet is given by

$$M_{max} = \frac{B_{max}^2 R^2 q^2}{2E}, \tag{3.6}$$

where $q = e$ for singly charged negative ions. Substituting the values of B_{max} and R into Equation 3.6, we obtain

$$M_{max} = \frac{156340}{E[keV]}. \tag{3.7}$$

At ORNL, the ions are accelerated to 200 keV for injection into the tandem typically. For E = 200 keV,

$$E_{max} \sim 782amu. \tag{3.8}$$

In order to reach large copper clusters of mass greater than 782 amu, lower ion energies must be used. For example, the Cu cluster of n = 50 has a mass of 3250 amu. The corresponding ion energy should be E $\leq$ 48 keV, according to Equation 3.7.

The mass analysis system is essential and must give the correct mass not only for the mass spectrometry result but also for the accelerator mass spectrometry tuning. For accelerator mass spectrometry, the ion energy E after acceleration in a tandem is

$$E = e\left(\frac{(V_i + V_t)M_p}{M_i} + qV_t\right), \tag{3.9}$$

where $V_i e$ is the energy of the ions injected into the accelerator, e is the electronic charge, V_t is the terminal voltage, M_p is the positive ion mass, M_i is the negative ion mass, q is the ion charge when leaving the terminal and is determined by the bending magnet(E in Figure 3.1). Only an ion beam with the right mass M and charge q is bended and accelerated down the tandem. M is controlled by the mass analysis system and q is selected by the bending magnet B from all the possible q the beam can have after passing through the stripper: given by Equation 3.5,

$$q^2 = \frac{2ME}{(BR)^2}. \tag{3.10}$$

To detect the ultra-trace-level ^{238}U and ^{232}Th, the beam needs to travel all the way from the ion source, the electromagnetic quadrupole lenses, the bending magnetic, and down to the energy analyzer magnet (E in Figure 3.1). It requires not only well controlling but excellent tuning. The electromagnetic quadrupole lenses which are used to focus the (negatively or positively) charged beam inside the AMS tandem need to be set appropriately for good tuning. To adjust the setting of these focus systems, a relatively higher intensity beam with the same charge and the same, or at

least close, mass to the interested beam is desired. Thus, to detect the ultra-trace-level ^{238}U and ^{232}Th by AMS, copper cluster Cu_4 beams is a good choice.

3.4 Sputter targets

Four different copper materials were used as the sputter targets: natural copper, ultra-pure copper, ^{63}Cu enriched copper and ^{65}Cu enriched copper.

Natural copper is a commercially available material in solid or power form with a natural abundance of copper 63 (69%) and copper 65 (31%) isotopes. The shape of the solid copper cone for SNICS (solid copper) is shown in Figure 3.6. Its size is 8 mm in diameter, 20 mm in height with $\sim$ 8 mm in diameter hemisphere surface.

The ultra-pure copper is electroformed and machined in the underground clean room especially for the MAJORANA project. This copper should be extremely pure with little contamination. It also contains the natural abundance of copper 63 and copper 65. The ^{63}Cu enrichment is 99.99%. Similarly, the ^{65}Cu enriched copper is 99.99%. Both enriched copper materials are in powder forms.

The sputter targets can be made from solid copper or copper powder. Figure 3.3 is a schematic view of the cathode with pressed powder sputter target. The solid targets are machined from solid copper materials and have the dimensions of 8 mm in diameter and 20 mm long, with a spherical surface curvature, as shown in Figure 3.6a. The solid target is directly threaded onto the water-cooled, removable rod. Figure 3.6b is a photo of the used sputter target.

3.5 Operation conditions

Our cesium sputter source was typically operated with the W-ionizer heated to about $1400°C$ for surface ionization of Cs vapor. The ionization efficiency for Cs was approximately 99.7%. The external Cs oven temperature was between $220°C$ to $250°C$, at which the Cs positive ion currents bombarding the cathode were on the

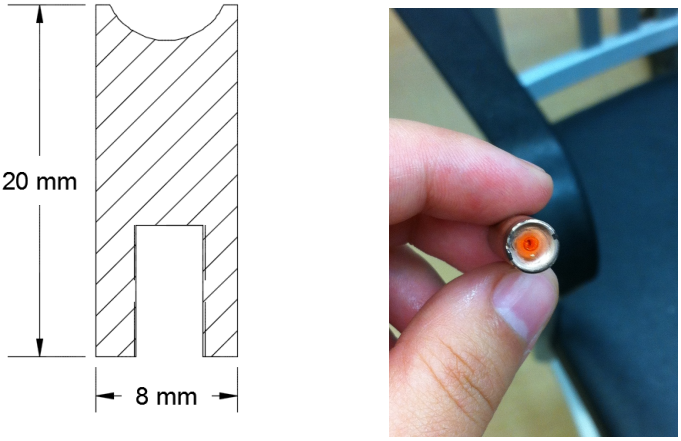

Figure 3.6: The solid copper target material for SNICS. The left figure is the shape of a new copper target and the right figure is a photograph of one used target. The target has 8 mm in diameter, 20 mm in height.

order of 0.5 mA. Sputter voltage between 1 kV to 8 kV were used to sputter the target. Negative ions were extracted from the ion source and accelerated to energies of 40 - 200 keV before being injected into the 90-degree dipole magnet for mass analysis. To reach large copper clusters of mass $\sim$ 3300 amu, an ion energy of 40 keV was used.

Chapter 4

Result and Discussion

The formation of negative copper cluster ion beams with a Cs-sputtering negative ion source was studied with different sputter targets and under different sputter conditions. Four types of sputter target materials have been used: (1) natural copper metal, (2) ultra-pure (UP) copper metal electro-formed in the underground clean room of the MJD project, (3) ^{63}Cu enriched (100%) powder, and (4) ^{65}Cu enriched (100%) powder. The sputtering voltage was varied between 1 to 8.5 kV at Cs^+ ion currents of $\sim$ 0.5 mA. The results are presented and discussed below.

4.1 Mass spectra

Figure 4.1 shows a typical mass spectrum of the negative ion copper clusters obtained with a natural copper target at 8 kV sputter voltage. The ions were accelerated to 40 keV energy. Ion peaks corresponding to masses up to 3000 amu have been obtained. Besides the peaks associated with copper clusters, various atomic and molecular ions were also present. In particular, another series of peaks was observed to intertwine with the Cu clusters, as shown more clearly in Figure 4.2, which became more intense than Cu cluster ions at masses higher than 2000 amu. The measured mass spectra were slightly out of calibration for high masses. Hence, in order to correctly identify the Cu clusters, the experimental data were re-calibrated by fitting. To do so, the

characteristic mass peaks of relatively small atomic and molecular anions, such as ^{16}O,$^{16}O_2$ and $^{63}Cu/^{65}Cu$, were identified first, and then the series of copper cluster peaks. A regression equation of the real mass as a function of the measured mass was established and fitted to the experimental data. All the mass spectra shown in this chapter are re-calibrated.

According to their fitted masses, the series of intertwined peaks are identified as molecular anions of Cu_n + O_2.The intensity of the Cu_nO_2 peaks varied strongly from sample to sample and also depended on the source operation parameters. They were also observed in the mass spectra of the ultra-pure copper targets which were made with electrolytic techniques in the underground clean room and one would expect a low oxygen content. It is, therefore, likely that the oxygen was coming from the ion source itself.

Similar sizes of copper clusters are also obtained with different copper materials. Figure 4.3, 4.4 and 4.5 presents the mass spectra of ultra-pure copper and ^{63}Cu enriched and ^{65}Cu enriched samples, at 8 kV sputter voltage.

Negative ion clusters extracted from Cs-sputter negative ion source have been reported [54].

All the mass spectra exhibit a number of common characteristic features. First, the Cu_n^- intensity decreases with increasing cluster size n and follows a power-law dependence. Second, there is an even-odd alternation an intensity variation phenomenon between neighboring clusters. Third, a discontinuity in the ion intensity is observed at specific cluster sizes n = 2, 8, 20, 40. These correspond to the magic numbers of the electrons of closed shells in the shell model. These features are discussed in the following Sections.

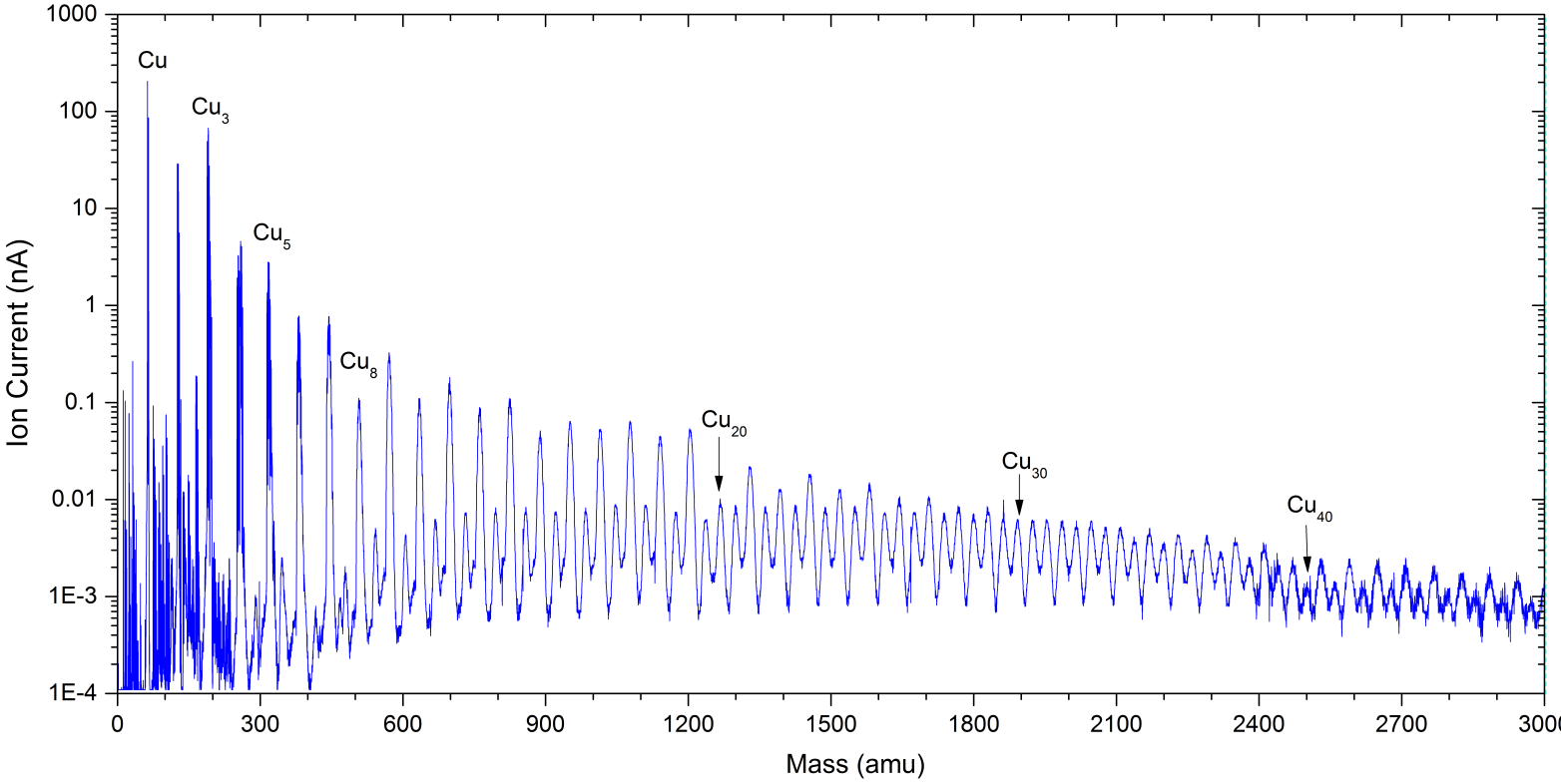

Figure 4.1: Mass spectrum of negative ions generated with a natural copper target and a sputter voltage of 8 kV.

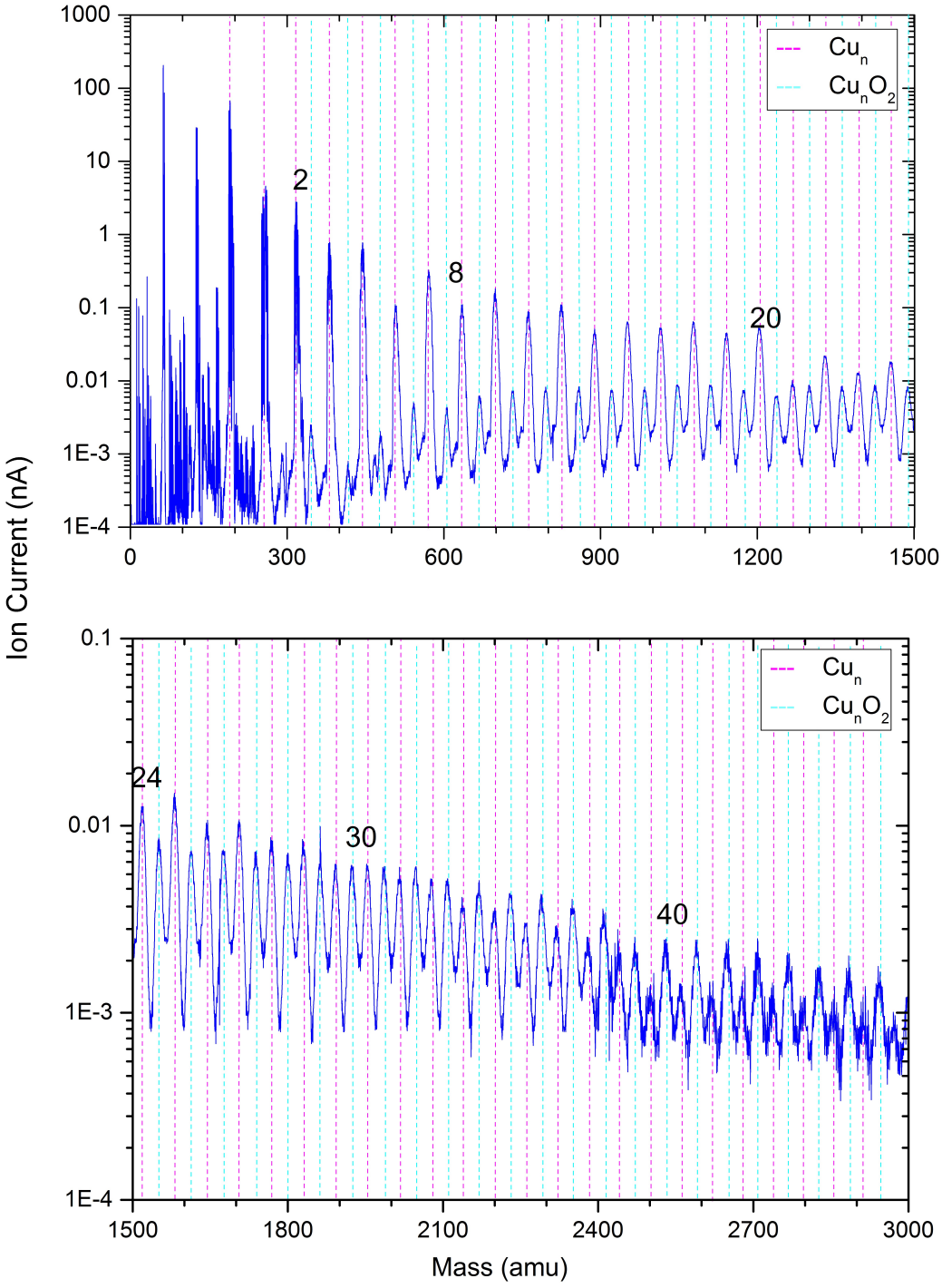

Figure 4.2: Mass spectra of copper clusters in the cluster range of (top) n = 1- 23 Cu atoms and (bottom) 24-47 Cu atoms generated with a natural copper target and a sputter voltage of 8 kV. $Cu_nO_2^-$ ions are observed between the Cu_n^- cluster peaks

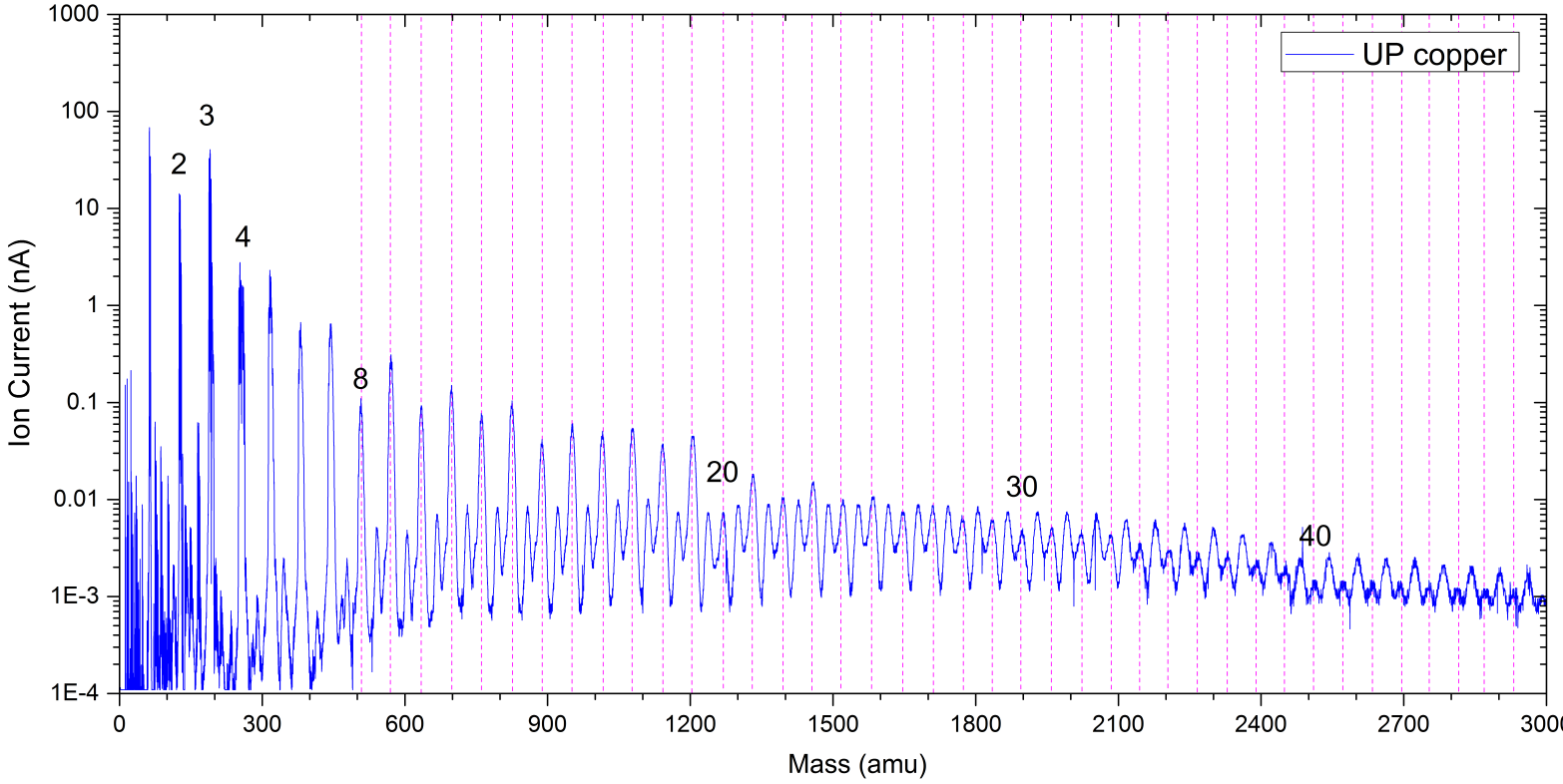

Figure 4.3: Mass spectrum of negative ions generated with a clean copper target and a sputter voltage of 8 kV.

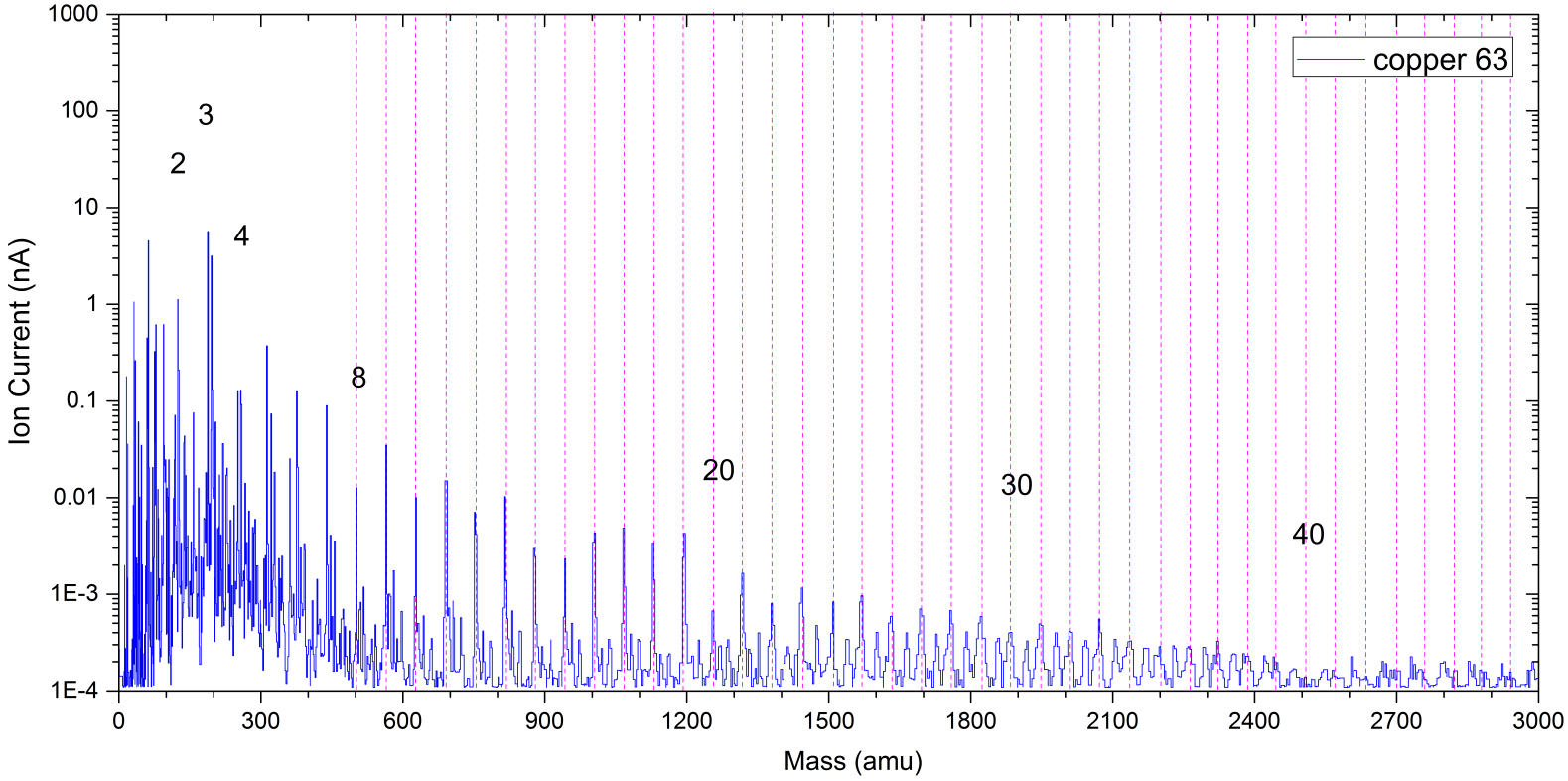

Figure 4.4: Mass spectrum of negative ions generated with a enriched copper 63 target and a sputter voltage of 8 kV.

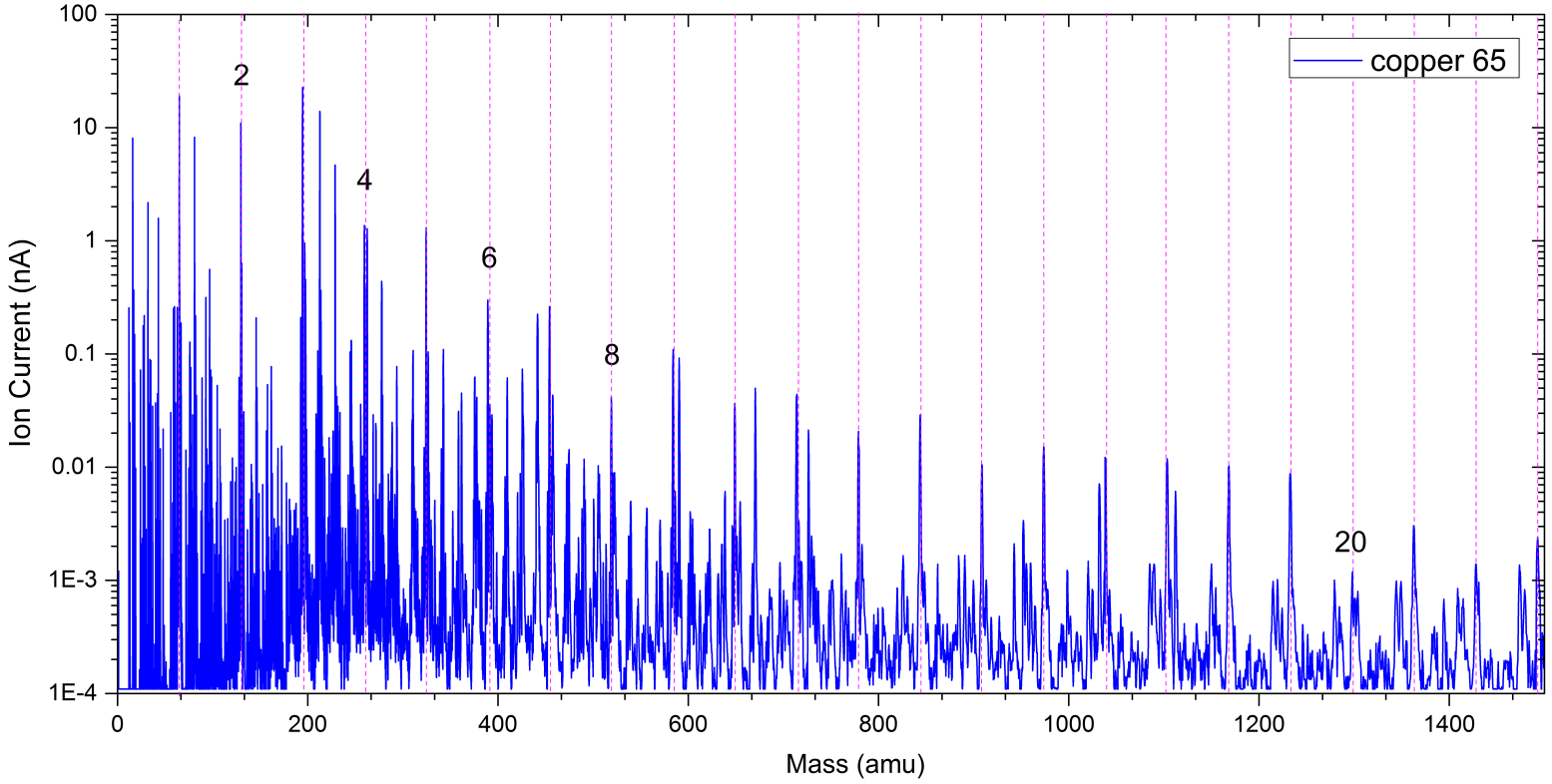

Figure 4.5: Mass spectrum of negative ions generated with a enriched copper 65 target and a sputter voltage of 8 kV.

4.2 Even-Odd alternation

One distinct characteristic of the mass spectra is the even-odd alternation: the negative ion intensity of an odd n clusters is larger than that of the adjacent even $n-1$ and $n+1$ clusters, as shown in Figure 4.2, 4.3, 4.4 and 4.5. For example, the intensity of negative copper cluster$n = 11$ is larger than the intensities of $n = 12$ and $n = 10$ clusters. The even-odd alternation has been observed in the coinage metal (such as Cu, Ag and Au) cluster ions generated under rare ions bombardment[19] as well as in other cluster ions, such as C clusters. Such behavior can be explained in terms of electron pairing in the highest occupied molecular orbitals (HOMOs). Copper atom has only one valence electron. Even (odd) neutral copper clusters have an even (odd) number of valence electrons and the HOMO is doubly (singly) occupied. The electrons in a doubly occupied HOMO have a stronger effective core potential than in a singly occupied HOMO. That is, the binding energy of the valence electrons is larger in a doubly occupied HOMO than in a singly occupied HOMO. For singly charged negative copper cluster ions, the odd clusters have a doubly occupied HOMO, while the even clusters have a singly occupied HOMO. Consequently, the observed even-odd alternation can be explained by two facts. First, the binding energy for the valence electron or electron affinity of copper cluster is relatively greater for odd-n clusters than for even-n clusters. Second, as discussed in Chapter 2, higher negative ion yields are expected for species with higher electron affinities.

Katakuse et al. observed the same even-odd alternation patterns in both negative and positive copper cluster ions, Figure 4.6, which can be considered as a good support to this explanation. The odd clusters have lower ionization potentials due to a singly occupied HOMO than the even clusters. Consequently, the even-odd alteration of the positive ion intensities can be understood by means of the even-odd alternation of the ionization potentials of the neutral Cu clusters.

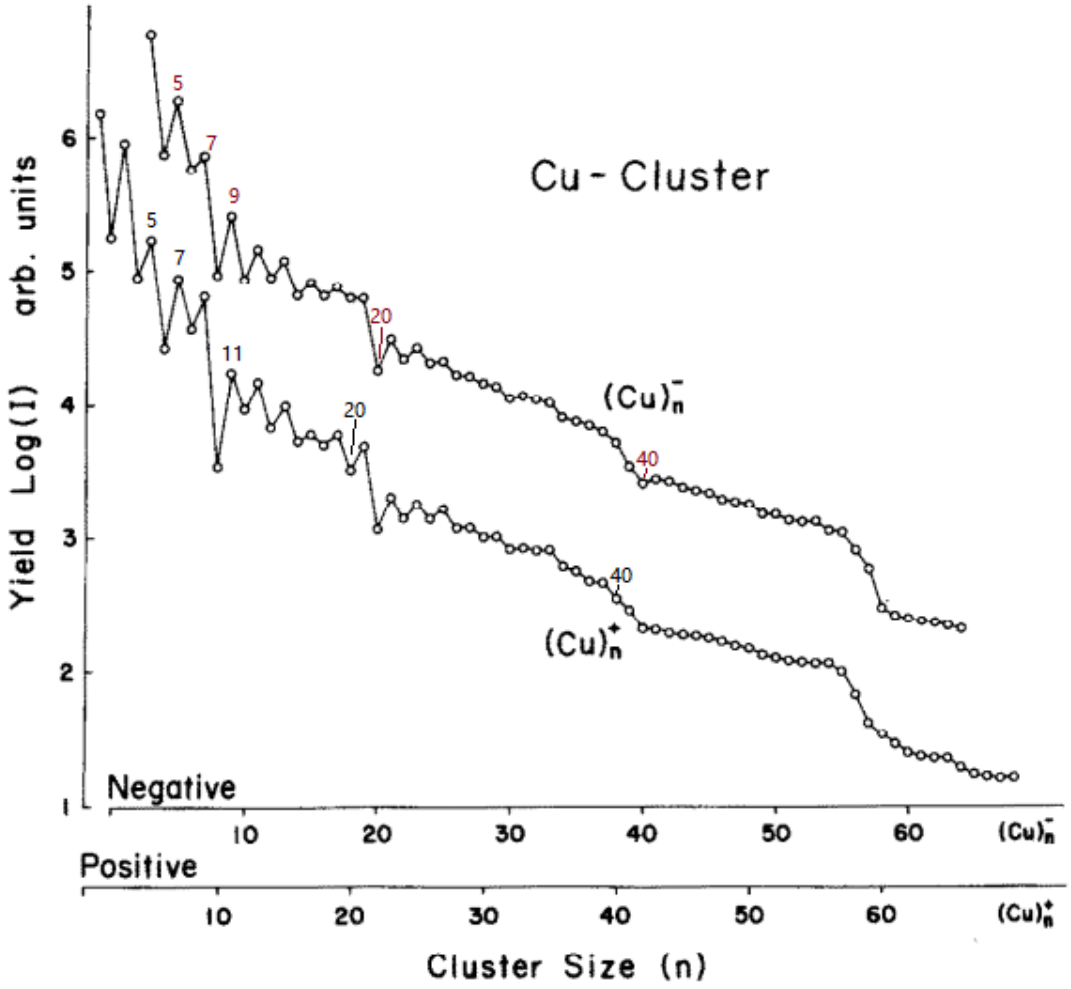

Figure 4.6: Mass spectra of copper clusters, Cu_n^- upper curve and Cu_n^+ lower curve. Adopted from [28].

4.3 Shell model

The mass distributions of Cu_n^- clusters possess major drops in intensity at n = 8, 20, and 40, as shown in Figure 4.1, 4.3, 4.4 and 4.5. These breaks have been explained by the shell model [27] as the shell closing effect and the cluster sizes at which the electron counts correspond to the closing of electronic shells are referred to as the magic numbers.

The copper clusters, as a kind of the metal clusters, are finite fermion systems whose bonding are provided by the delocalized valence electrons. The delocalized valence electrons dominate the quantum properties of copper clusters and brings a nuclei-like shell structure. Researchers noticed that the behavior that the detailed ionic structure often does not seem to affect very much the properties of copper cluster. Actually, as Christensen [8] showed, the important quantity governing properties of the cluster ground-state structure such as energy fine structure, electronic level spectra, and geometry is the number of delocalized electrons rather than the number of atoms in the cluster.

Considering a copper atom has 29 proton and one valence electron, a simple approach of shell model is one-electron shell model in which independent delocalized atomic 4s electrons are bound in a spherically symmetric potential. In this approach, each valence electron is described as a free independent particle moving in the spherical potential field produced by the smeared structureless positive charge density of the N ion cores and the average potential of the N-1 other electrons in the cluster. The simplest spherically symmetric potential is square well potential. Thought square well potential is theoretical ideal potential, it explains the magic number 2, 8, 20, and 40 we observed:

based on classical quantum mechanics, the allowed energies for three square well is

$$E_{nl} = \frac{\hbar^2}{2ma^2}\beta_{nl}^2, \tag{4.1}$$

and the wave functions are

$$\psi_{nlm}(r,\theta,\phi) = A_{nl} j_l(\beta_{nl} r/a) Y_l^m(\theta,\phi), \tag{4.2}$$

where β_{nl} is the n^{th} zero of the l^{th} spherical Bessel function; A_{nl} is the normalization constant; $j_l(r)$ is the spherical Bessel function and $Y_l^m(\theta,\phi)$ is the spherical harmonics. n = 1, 2, 3 ...; l = 0, 1, 2, ..., n-1 and m = -l, -l + 1, ..., -1, 0, 1, ..., l - 1, l. These three quantum numbers are also known as n principal, l angular momentum and m magnetic. For each value of l, there are (2l + 1) different values of m. Considering the spin $s = 1/2$, each energy level is 2(2l + 1)-fold degenerate.

The degeneracy of $N_{nl} = 2(\ 2l + 1)$ gives Table 4.1.

Table 4.1: Degeneracy table of square well potential

N_{nl}	degeneracy $2(2l+1)$	states under or on
1s	2	2
1p	6	8
1d	10	18
2s	2	20
1f	14	34
2p	6	40
1g	18	58
2d	10	68
1h	22	90

In negative secondary ion mass spectrometry, only sputtered particles with negative charge are accelerated, mass analyzed and measured. Therefore, the number of free electron in mass analyzed $n-mer$ (the copper cluster with n atoms) are n+1. For $n-mer$ with n equals the magic number n_s, it contains a single extra electron at the highest energy level /shell with relatively lower bonding with the atoms. In other words, $n_s - mer$ has relatively higher probability to lost the charging electron and not be measured. $(n_s + 1) - mer$ has two electrons at the highest energy level /shell. Considering the electron-pairing effect, $(n_s+1) - mer$ is relatively stable than

Table 4.2: Shell-closing effect observed in the mass spectra of the negative copper clusters. The shell-closing effect is observed at the $(n_s - 1)$-mer, where n_s is the shell-closing number. Adopted form [28]

n_s	Configurations	$(Cu)_n^-$
2	$1s$	○
8	$1p$	○
18	$1d$	△
20	$2s$	○
34	$1f$	△
40	$2p$	○
58	$1g$	○
92	$2d, 1h, 3s$	○

○= observed clear shell-closing effect.
△= observed weak shell-closing effect.

$n_s - mer$. Therefore, $n_s - mer$ are the discontinuity points in negative secondary ion mass spectrometry and have relatively lower intensity than its neighbors.

Table 4.2 shows the shell-closing number(n_s) of the electrons in the square well potential with finite walls and the shell-closing effects observed in our experiments. The observation of magic number 58, 92 and 138 in a copper cluster mass spectrum, according to [28]), comments that the square well potential is more likely to describe the interaction that the atoms inside a cluster suffered than harmonic oscillator.

The other spherically symmetric potential is also allowed, such as Harmonic Oscillator. Figure 4.7 summarize the predictions given by Harmonic Oscillator potential, square well potential and intermediate potential.

4.4 Binomial distribution

Examination of the mass spectra obtained with national copper samples showed that small clusters ($n < 9$) consist of an ensemble of multiple resolved peaks, as illustrated in Figure 4.8. This is explained by the fact that natural copper has two isotopes ^{63}Cu and ^{65}Cu, which gives rise to more than one species of composition $^{63}Cu_x{}^{65}Cu_{n-x}$ for the cluster containing a total of n Cu atoms. The relative intensities of the

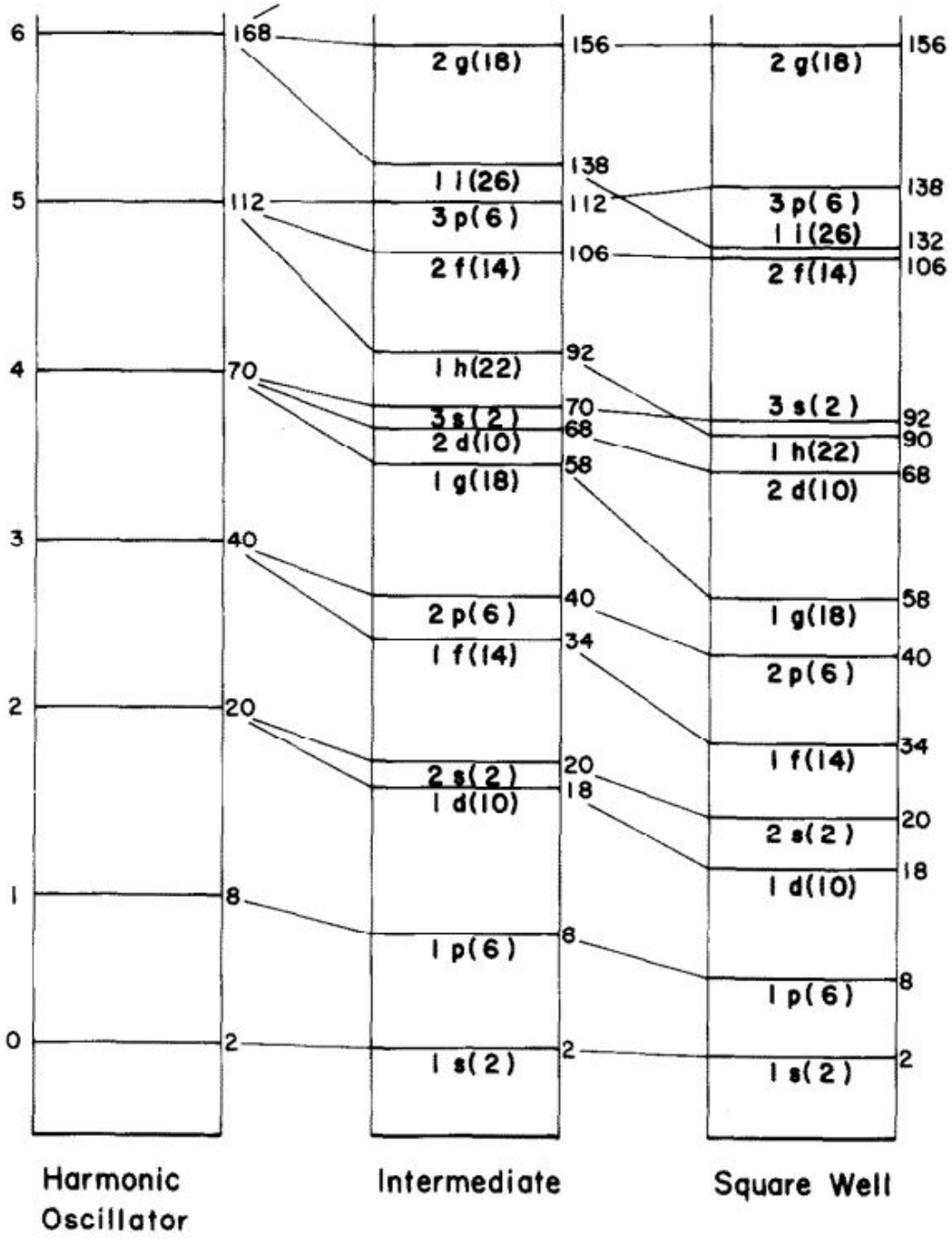

Figure 4.7: Energy levels of the electrons trapped in a harmonic oscillator, a square well and an intermediate potential between them. Adopted form Katakuse et al. [28].

$^{63}Cu_x{}^{65}Cu_{n-x}$ compositions are found to follow a binomial distribution given by

$$F(n,x) = p^x(1-p)^{n-x}\frac{n!}{x!(n-x)!}, \tag{4.3}$$

where $F(n,x)$ is the fraction of cluster $^{63}Cu_x{}^{65}Cu_{n-x}$ with x ^{63}Cu atoms in the cluster of n total Cu atoms, $p = 0.6917$ (the natural abundance of ^{63}Cu) is the probability that an copper atom is ^{63}Cu, and $(1-p)$ is the probability for an atom of ^{65}Cu. Figure 4.8 and 4.9 shows the measured mass spectra of n = 422 clusters and the calculated relative intensities for the compositions in terms of a binomial distribution using Equation 4.3. The binomial distributions are normalized to the maximum peak of the experimental data for each cluster. As noted, the experimental ion distributions agree well to the respective binomial distributions. For $n > 8$, the cluster compositions are no longer resolved in the mass spectra, but the envelopes of the cluster ensembles could still be described by binomial distributions (Figure 4.9). The mass resolution can be increased by reducing the slit widths of the mass analyzing magnet, at the expense of the ion intensity. Such a high resolution mass spectrum is presented in Figure 4.10 for the cluster n = 9, in which the $^{63}Cu_x{}^{65}Cu_{9-x}$ compositions are well resolved and fit to a binomial distribution.

Binomial distributions have been observed in many clusters of binary compositions such as GaAs [37] and metal alloys [26, 58] Deviations from binomial distributions are also observed [29, 37], which indicate the occurrence of preferred cluster formation or ejection for certain components or kinetic effects in the cluster formation process [37]. In our study, the composition of the natural Cu clusters are found to be best described by the binomial distribution, suggesting the following cluster growth mechanism in the sputter process: it involves random multiple sequential aggregations; the ^{63}Cu and ^{65}Cu atoms can be bind equally during the growth procedure, and the probability to add one ^{63}Cu or ^{65}Cu atom is proportional to their natural abundances at the sputter surface. This is not surprising as the two isotopes are of the same element. As expected, no binomial distributions were observed in the mass peaks from enriched

h

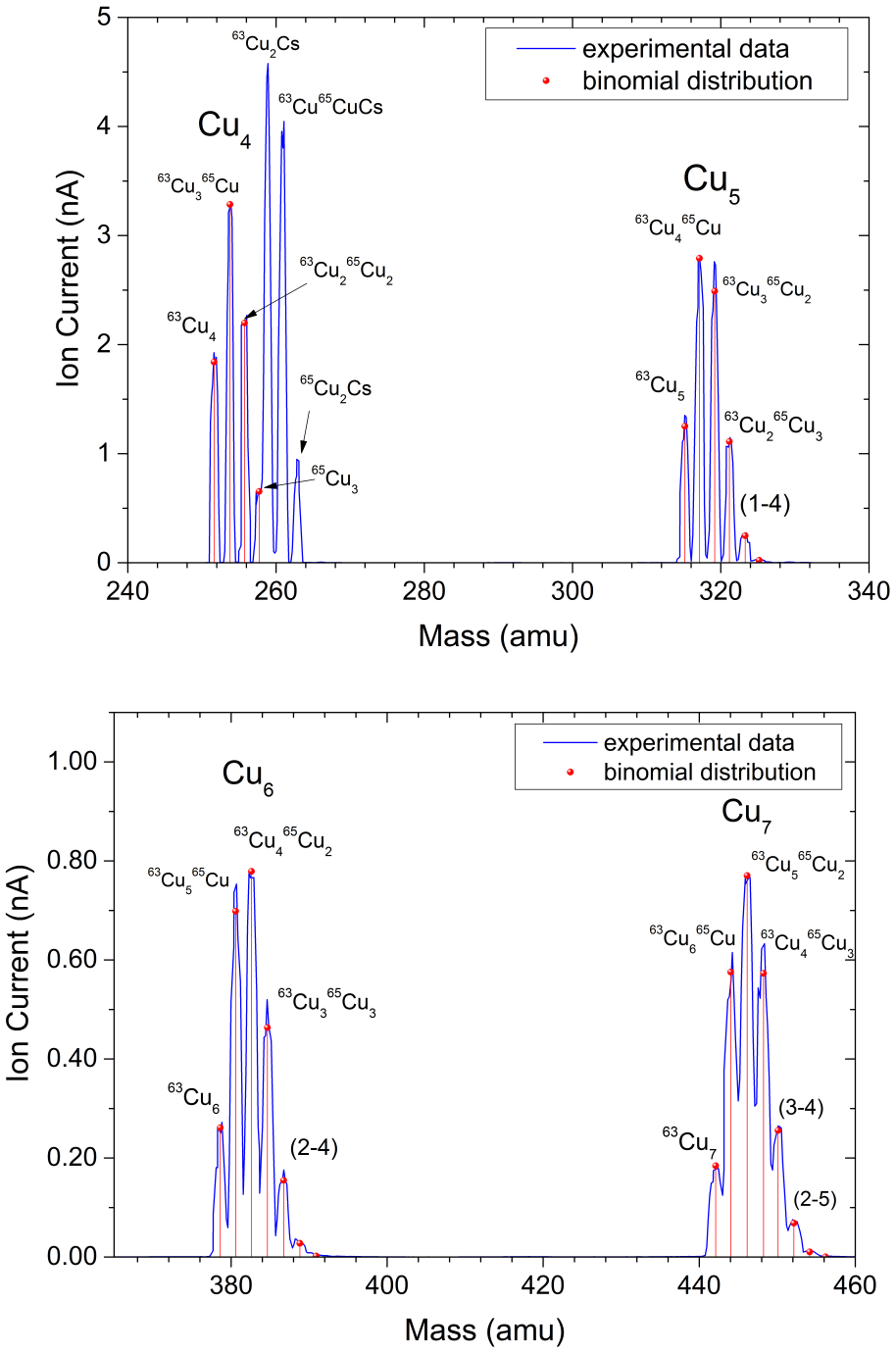

Figure 4.8: Measured ion compositions of n = 4 7 clusters and the corresponding binomial distributions predicted by Equation 4.3 (a) n = 4 and 5, and (b) n = 6 and 7. The blue lines are experimental data and the red dots are the binomial distributions normalized to the experimental data.

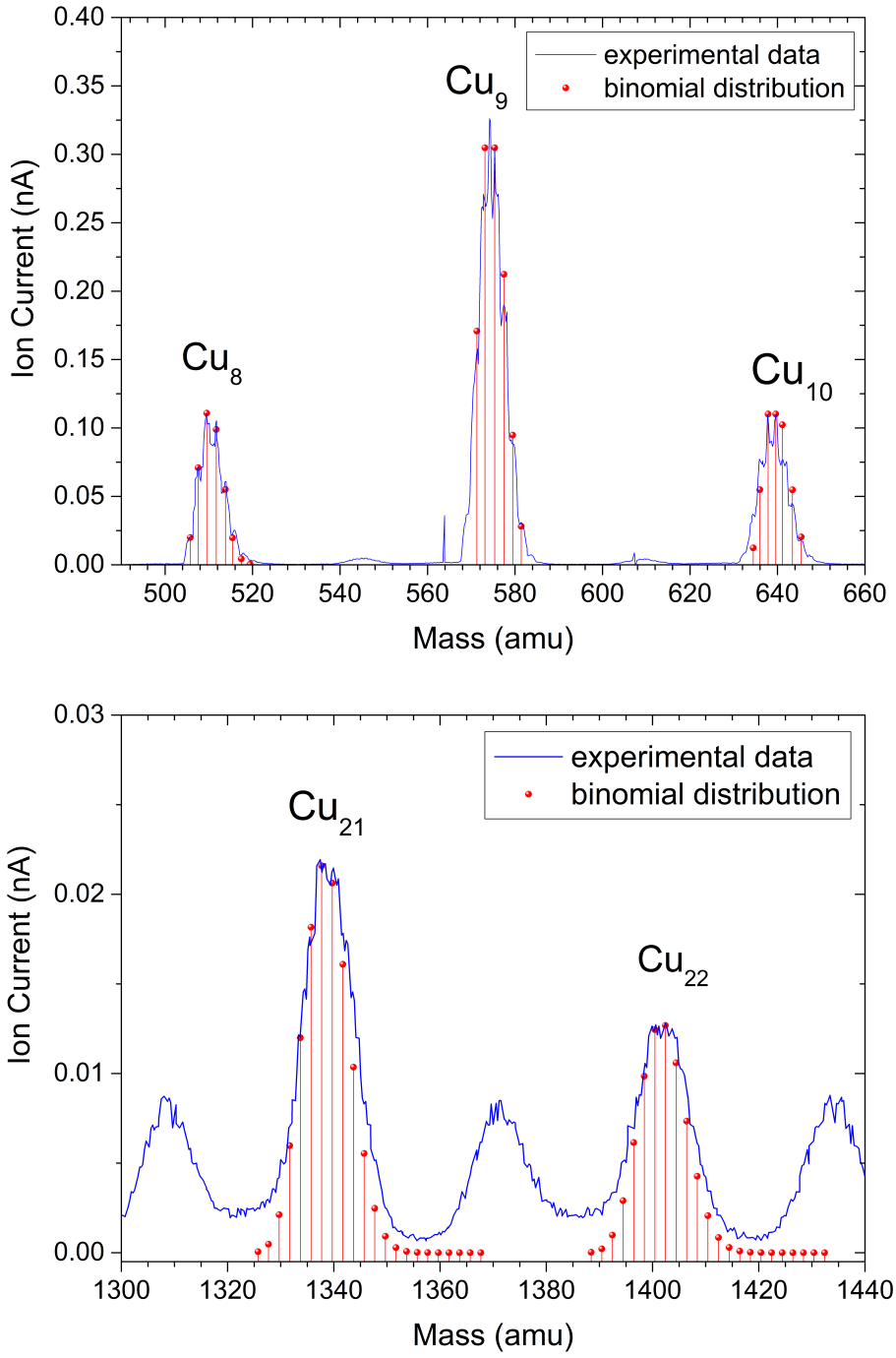

Figure 4.9: Measured ion compositions of n = 8 - 10 and 21, 22 clusters and the corresponding binomial distributions predicted by Equation 4.3 (a) n = 8 - 10, and (b) n = 21 and 22. The blue lines are experimental data and the red dots are the binomial distributions normalized to the experimental data.

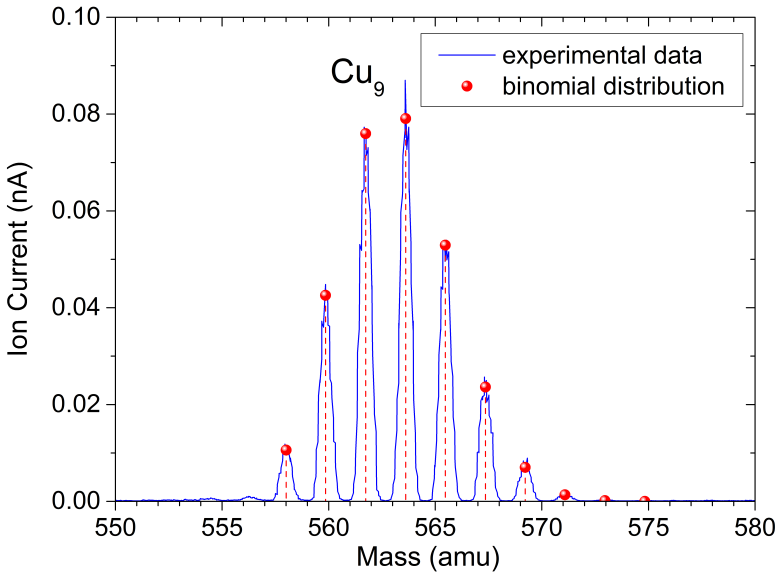

Figure 4.10: High-resolution mass spectrum of natural copper cluster $n = 9$ and its binomial distribution.

^{63}Cu and ^{65}Cu samples, since these two materials have only one isotope and thus one possible composition for each cluster. (Figure 4.11)

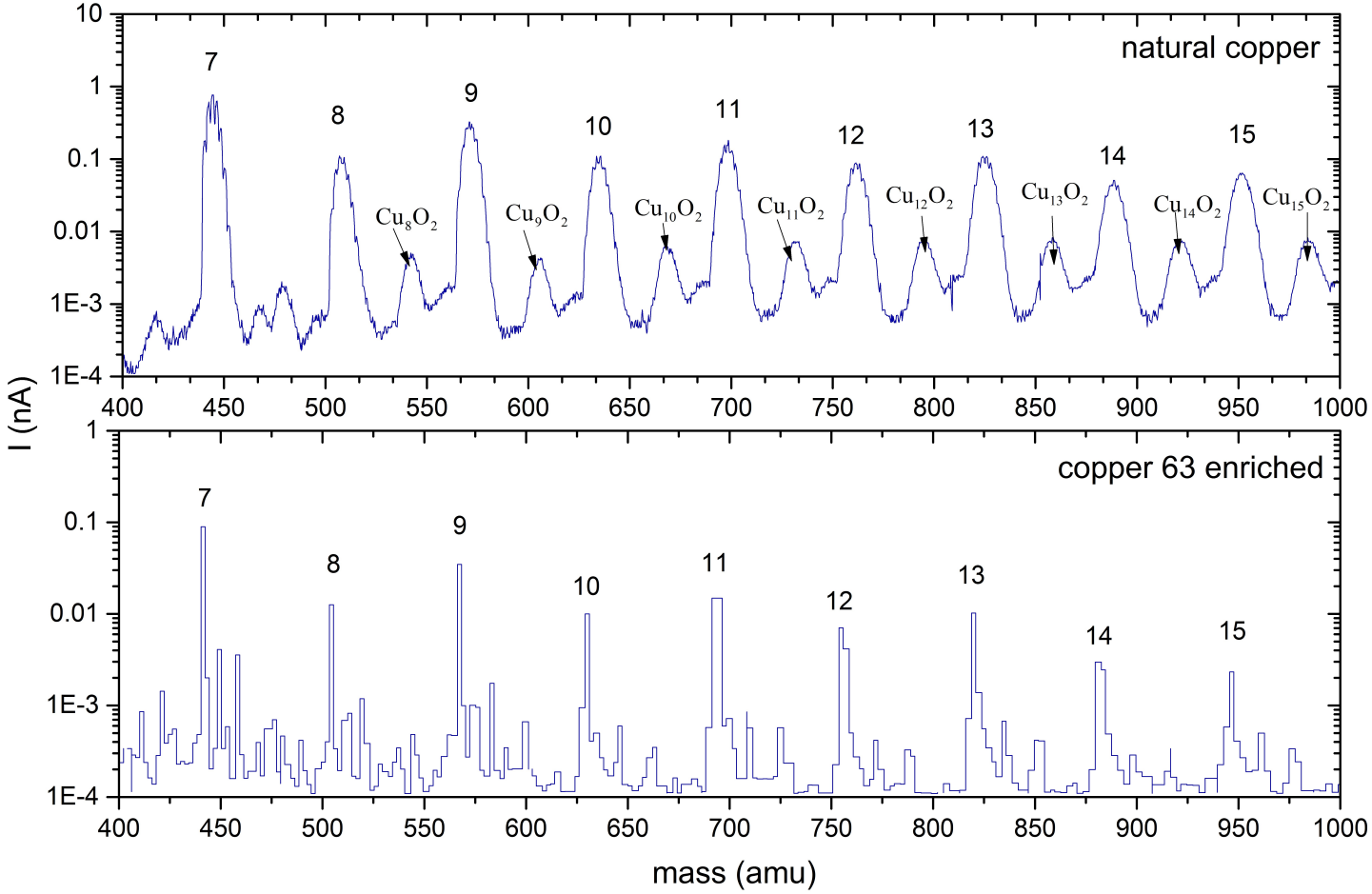

Figure 4.11: Measured ion compositions of n = 7 to 15 copper clusters produced with natural copper (upper) and ^{63}Cu enriched copper (lower).

4.5 Power law dependence

4.5.1 Sputter yield

As shown in Figure 4.1, 4.3, 4.4 and 4.5, the intensity of sputtered Cu_n^- clusters decreases with size n. It has been reported [13, 57] that the decreasing follows a power law dependence:

$$Y_n \propto n^{-\alpha} \tag{4.4}$$

where Y_n the yielding (intensity) of the cluster n and α is a condition constant which we discussed in section 2.2.1.

The power-law dependence has been observed in the Cu_n^- clusters obtained in this study. In order to determine the value, careful data analysis is necessary and the methods discussed below are employed.

4.5.2 Relative cluster yields

The sputter yield is dependent on the ion source operating conditions such as the sputtering voltage, Cs oven temperature, W-ionizer temperature, etc. In addition, the measured ion intensity after mass separation is sensitive to the beam turning condition which affects the beam transmission to the Faraday detector. In order to compare the experimental data obtained under different operating conditions, we introduced normalized sputter yield or the relative sputter yield Y_n^{rel} defined as

$$Y_n^{rel} = \frac{I_n}{I_1}, \tag{4.5}$$

where Y_n^{rel} is the relative yield of cluster Cu_n^- of size n, I_n is the ion intensity of Cu_n^- and I_1 is the ion intensity of Cu^- (n=1). For enriched ^{63}Cu and ^{65}Cu samples, each cluster has only one mass peak and I_n is the ion intensity of the corresponding mass.

4.5.3 Intensities of binomial mixed clusters

The determination of Y_n^{rel} is more complex for natural and ultra-pure copper data due to the presence of ^{63}Cu and ^{65}Cu isotopes. As discussed in Section 4.4, a Cu cluster of size n consists of a binomial distribution of $^{63}\mathrm{Cu}_x{}^{65}\mathrm{Cu}_{n-x}$ compositions. Therefore, the total intensity (yield) of cluster size n is the sum of all these sub-peaks:

$$I_n = \sum_{x=0}^{n} I_{^{63}Cu_x{}^{65}Cu_{n-x}}. \tag{4.6}$$

Due to contaminations in the ion source, the Cu mass spectra are often mixed with ion peaks of other elements. For instance, Cu_4 is partially overlapped with Cu_2Cs, as shown in Figure 4.8a, so that the intensity of sub-peak $^{65}Cu_4$ could not be accurately determined. Further, the mass peaks of larger Cu clusters ($n > 14$) are increasingly overlapped with the Cu_nO_2 peaks, making it difficult to obtain the I_n values for those large Cu clusters.

To solve this problem, the binomial distribution is considered. Since the composition of $^{63}\mathrm{Cu}_x$ $^{65}\mathrm{Cu}_{n-x}$ has a binomial distribution, the total intensity I_n of cluster n can be obtained from the intensity of one of the sub-peaks divided by the binomial fraction for that component. That is,

$$I_n = \frac{I_{^{63}Cu_x{}^{65}Cu_{n-x}}}{F(n,x)}, \tag{4.7}$$

where $I_{^{63}Cu_x{}^{65}Cu_{n-x}}$ is the relative intensity of the $^{63}Cu_x^{65}Cu_{n-x}$ peak and $F(n,x)$ is is the corresponding binomial fraction from formula 4.3.

For small clusters of $n < 8$, more than one components are resolved(Figure 4.8). The value of I_n is given as the average of the calculated yields for all resolved sub-peaks:

$$\bar{I_n} = \frac{\sum\limits_{x=x_1,x_2,\ldots x_L} \dfrac{I_{^{63}Cu_x{}^{65}Cu_{n-x}}}{F(n,x)}}{L}, \tag{4.8}$$

with L is the number of identified sub-peaks and x_i is the number of ^{65}Cu atoms in i^{th} identified sub-peak for a given cluster size n. (See Table 4.3 for example.)

For clusters of size $8 < n < 30$, the individual components are no longer resolved. The value of I_n is obtained using the peak ion intensity, I_{peak}, of the ensemble divided by the maximum fraction $F(n,x)_{max}$ of the binomial distribution for given n:

$$I_n = \frac{I_{peak}}{F(n,x)_{max}}. \tag{4.9}$$

For larger clusters ($n > 30$), Cu_n^- peaks are overlapping with the $Cu_nO_2^-$ peaks. The peak intensity I_{peak} is determined by fitting the overlapping ion peaks to a sum of Gaussian peaks, as illustrated in Figure 4.12. For large n, a binomial distribution can be reasonably approximated by a Gaussian distribution.

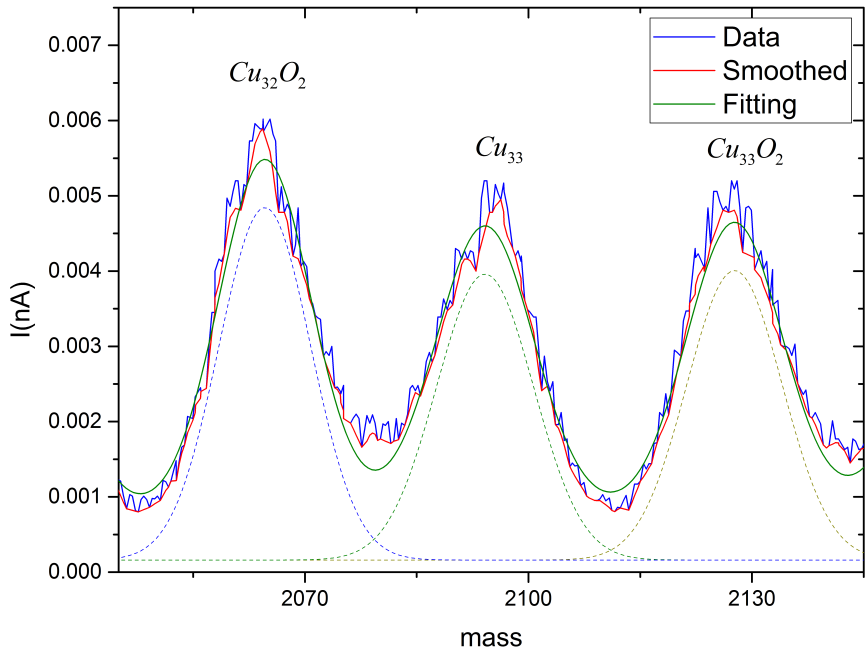

Figure 4.12: An example of multi-peak Gaussian fitting for cluster n = 33.

Table 4.3 lists the I_n values for $n \leq 14$ clusters obtained by direct summation of the ion peaks (Equation 4.6) and by using the binomial distributions (Equation 4.8 or Equation 4.9). As noted, the two methods are in excellent agreement for clusters

of $n < 10$. For $n \geq 10$, the discrepancies between the two methods are larger because the summed intensities are less accurate due to un-resolved sub-peaks. Therefore, the I_n values for natural and ultra-pure copper data are obtained using the binomial method (Equation 4.8 and 4.9).

Table 4.3: Intensities of Cu_n^- clusters with natural ^{63}Cu and ^{65}Cu isotopes. Column 2 is the number of sub-peaks identifiable in the clusters. Column 3 is obtained by summation of the sub-peaks. Column 4 is obtained using the binomial distributions. Column 5 gives the relative differences of two the methods.

n	Number of identified peaks L	I_n (Sum method)	I_n(Binomial method)	Relative difference
1	2	290.7	296.0	1.79%
2	3	63.15	60.51	-4.18%
3	4	148.4	151.9	2.40%
4	4	8.245	8.052	-2.34%
5	6	8.354	7.914	-5.26%
6	6	2.537	2.387	-5.90%
7	7	2.550	2.438	-4.38%
8	5	0.3692	0.3802	2.98%
9	6	1.047	1.130	7.90%
10	7	0.4998	0.4135	-17.26%
11	9	0.7971	0.7173	-10.01%
12	8	0.4173	0.3795	-9.05%
13	9	0.5938	0.4678	-21.22%
14	7	0.2451	0.2250	-8.20%

4.5.4 Analysis results

Figure 4.13 shows the relative yields of Cu_n^- clusters obtained from four different samples sputtered by 8 keV Cs^+. The curves can be fit to the power law given by Equation 4.4. Figure 4.15 shows the power-law fittings for the four curves. The values obtained are between 2.5 and 4.4 and are summarized in Table 4.4 .

Figure 4.16 shows the relative Cu_n^- yields obtained from natural Cu samples under different sputter voltages: V_{sp} = 3 - 8 kV. The power-law dependence is also established for these clusters and the corresponding exponents are $\alpha \sim 4.4$ for V_{sp}

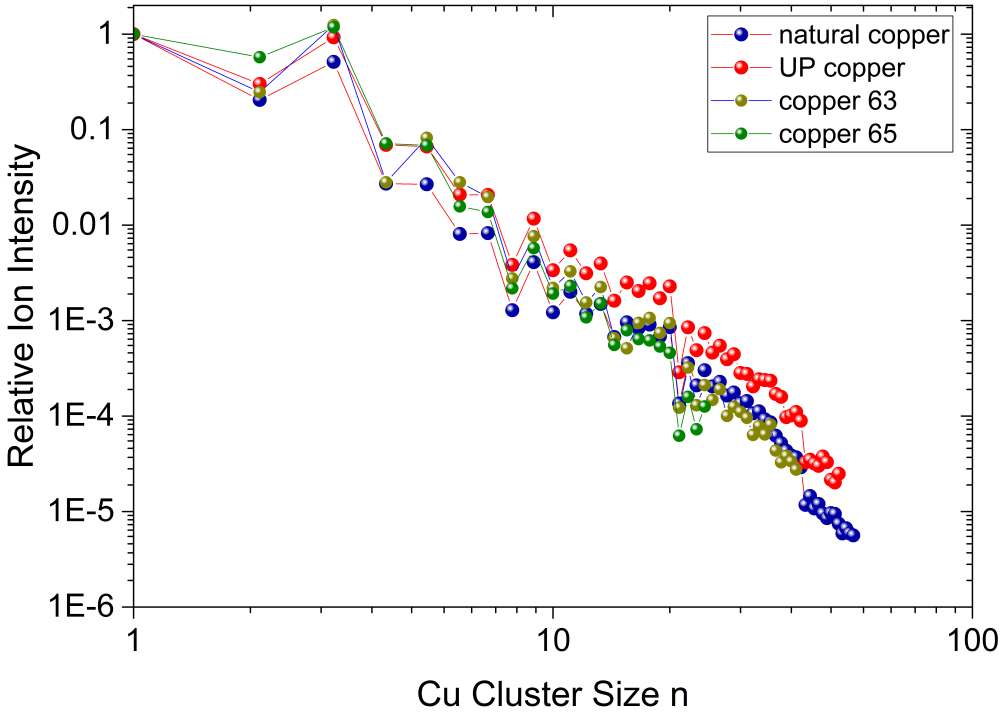

Figure 4.13: Relative yields of Cu_n^- clusters from four different sputter samples: natural copper, ultra-pure copper, ^{64}Cu enriched, and ^{65}Cu enriched coppers. Sputter voltage is 8 keV.

Table 4.4: The fitted power-law exponents α for the Cu cluster yields obtained with different copper samples and different sputter voltages V_{sp}. N_{max} is the max cluster size.

Sample	V_{sp} (kV)	α	N_{max}
Natural Copper	8	3.2 ± 0.1	52
UP Copper	8	3.1 ± 0.1	48
63Cu enriched	8	3.2 ± 0.1	38
65Cu enriched	8	3.4 ± 0.1	23
Nature Copper	6	2.5 ± 0.2	10
Nature Copper	3	4.4 ± 0.2	21

= 3, ∼2.5 for V_{sp} = 6 kV and are ∼ 3.2 for V_{sp} = 8 kV. The results are also listed in Table 4.4. For the measurements at V_{sp} = 3 - 6 kV, the ions were accelerated to higher ion energies (100 keV). This has limited the accessible mass ranges, due to the magnetic rigidity of the mass separation magnet, to cluster sizes of n 10 Cu atoms,

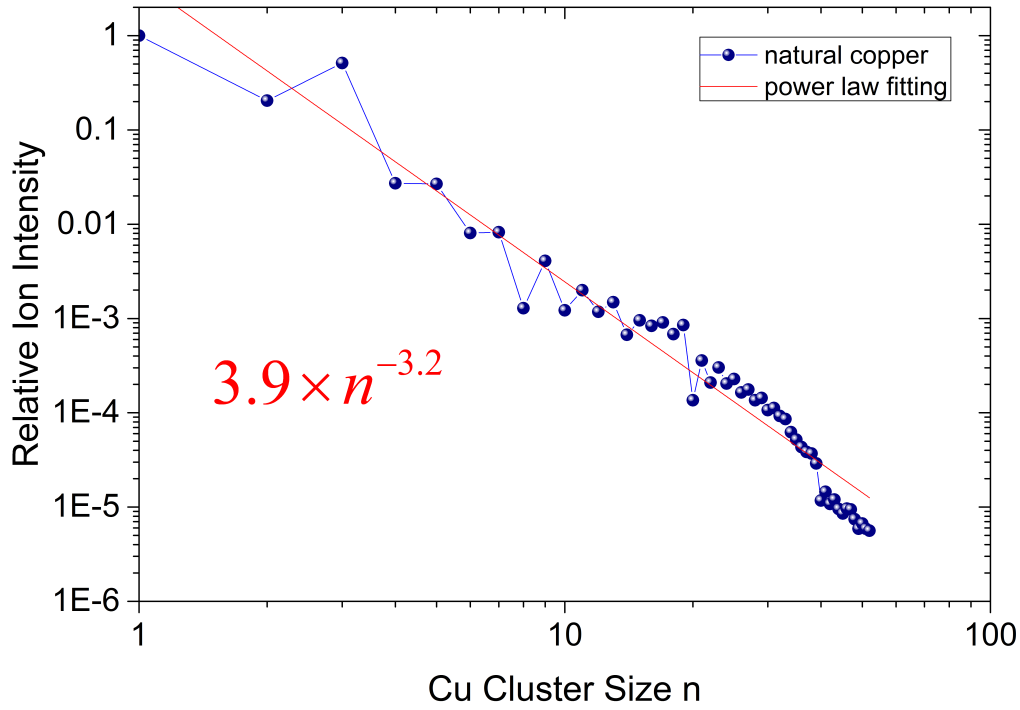

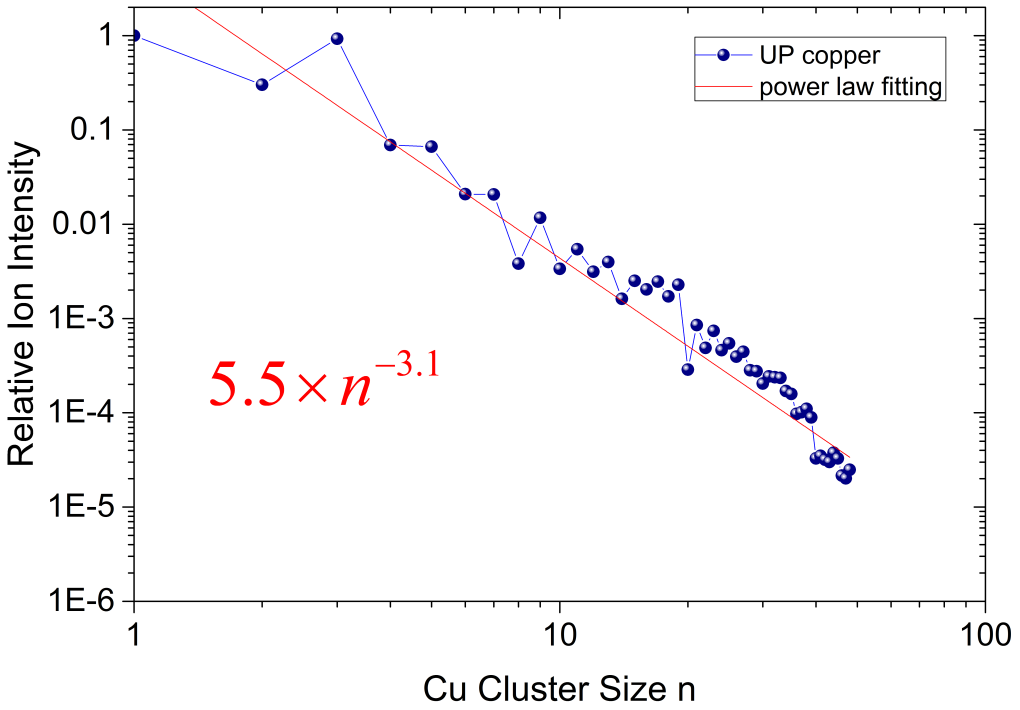

Figure 4.14: Power law dependences of Cu cluster from sputter samples: natural copper ($\alpha = 3.2$) and clean copper ($\alpha = 3.1$).

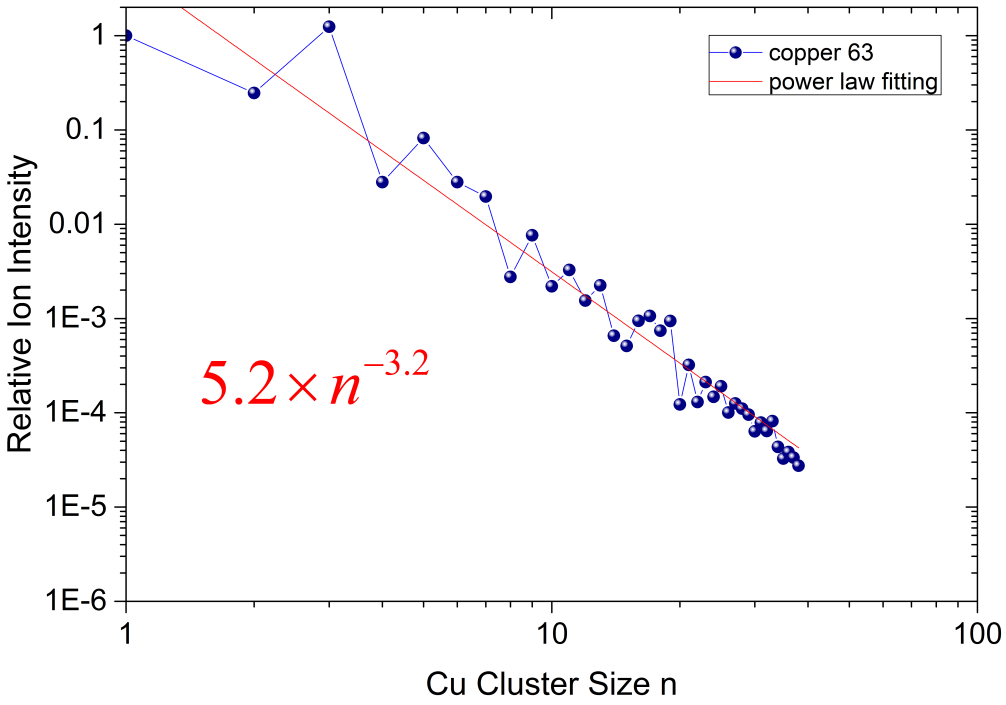

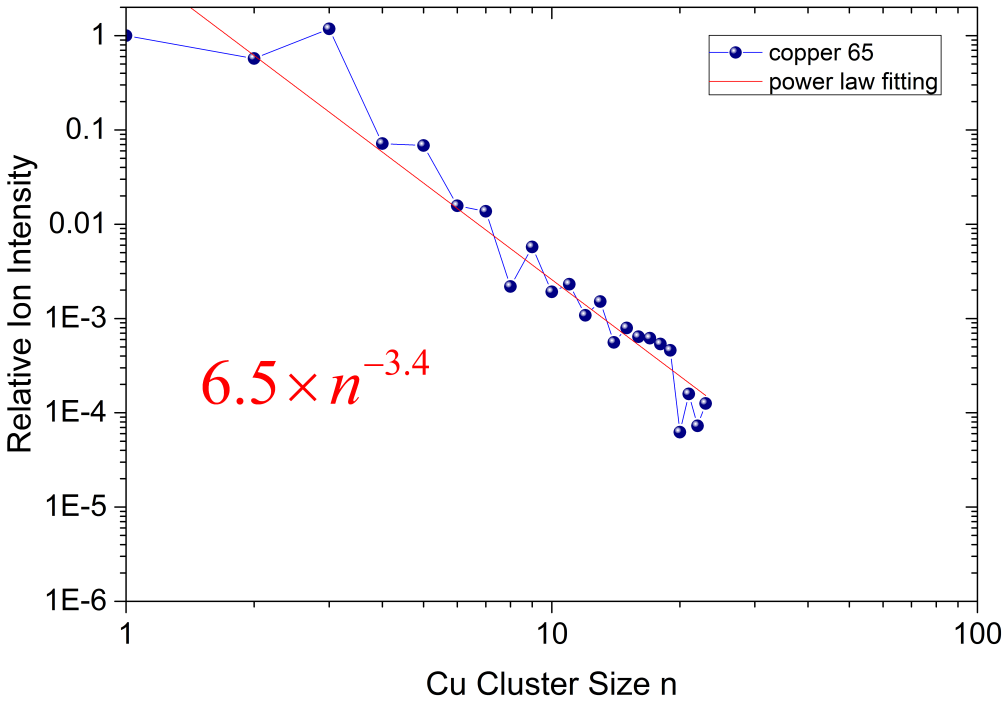

Figure 4.15: Power law dependences of Cu cluster from sputter samples: enriched copper 63 ($\alpha = 3.2$) and enriched copper 65 ($\alpha = 3.4$)

although larger Cu clusters were produced. The value of α should be related to the cluster formation process, as discussed below.

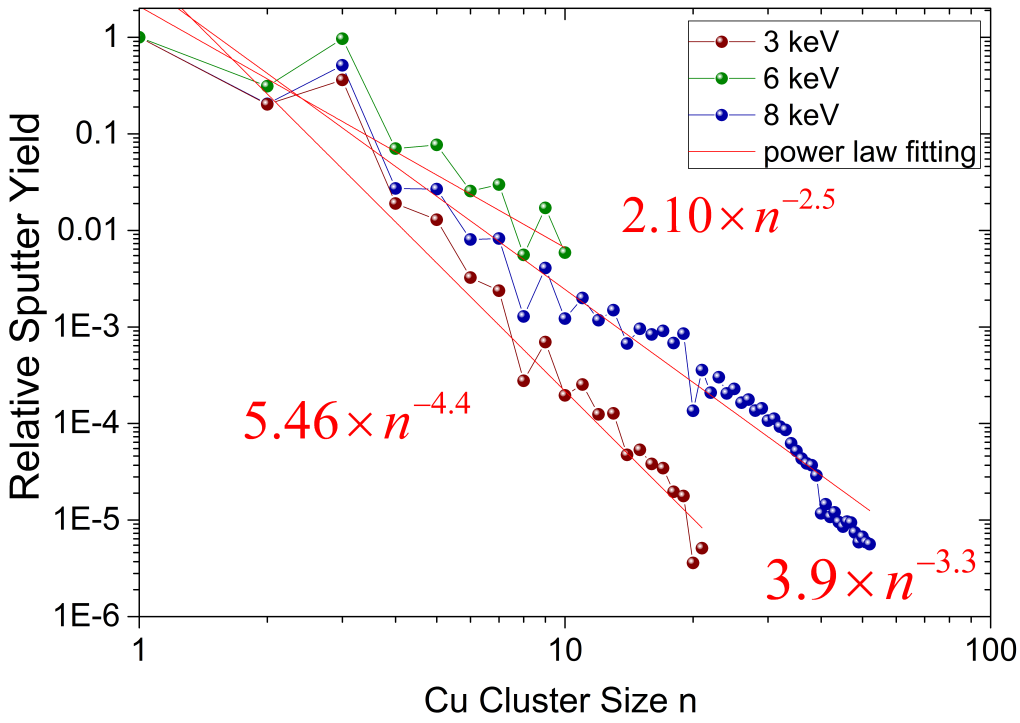

Figure 4.16: Intensity for natural copper clusters short mass scan for different sputtering energies.

4.5.5 Discussions

The values for the Cu_n^- cluster yields obtained with four different samples at sputter voltage V_{sp} = 8 kV are in the range between 3.1 and 3.4. A large range of values have been reported for Cu clusters: for example, α = 6.2 8.2 by Coon et al[12, 13] for neutral Cu clusters sputtered by Ne^+, Ar^+ and Xe^+ ions of 3.75 3.9 keV; α = 6.7 for Cu clusters sputtered by 5 keV Ar^+ ions [11], and α= 3.82 for sputtering with 15 keV Ar^+ ions [29]. However, in these previous studies, the Cu clusters produced are much smaller ($n \leq 17$) than those of the present study. Katakuse et al. obtained positive and negation Cu clusters up to sizes $n \sim 70$ (Figure 4.17) with 10 keV Xe^+

ion bombardment, but the power-law dependence was not reported. By overlapping Katakuses data with power-law dependence curves of different exponent values, as illustrated in Figure 4.17, one can see that the exponent α should be between 2 and 3 for Katakuses data. It is even smaller than the α values of our data.

The different exponent values may be attributed to the different sputter yields in different studies. In general, materials with higher sputter yields are expected to form larger clusters and thus have a smaller value of α. This has been reported by Coon et al. [13] as shown in Figure 4.18. Comparing the Cu clusters obtained in our studies and those in the prior works of [11, 13] ($\alpha = 6 - 8$), we obtained much larger Cu clusters (n $\sim$ 47) than the prior works, indicating significantly higher sputter yields in our experiments. Hence, smaller values of α can be expected. On the other hand, Katakuse et al. obtained larger Cu clusters than our experiments, which implies higher sputter yields and thus a smaller value than that of our data.

A number of theoretical models have been proposed for cluster formation in sputtering and are able to predict the power- dependence [4, 5, 52, 55]. Some of them [4, 55] predicted α on the order of $3.9 - 4.5$ for Cu_n clusters sputtered by 5 keV Ar^+, while some models predicted smaller values of α. For instance, the shock wave model [5] suggests an value around 2. The thermodynamic equilibrium model [52] gives $\alpha \sim 7/3$. Our experimental results seem to agree with the shock-wave and thermodynamic models. However, our results are not sufficient to provide experimental evidence to support any theoretical models. More systematic studies and more experimental data are necessary. Future studies will be focused on a better understanding the negative cluster ion formation mechanisms under Cs^+ sputter conditions and on producing more and larger clusters.

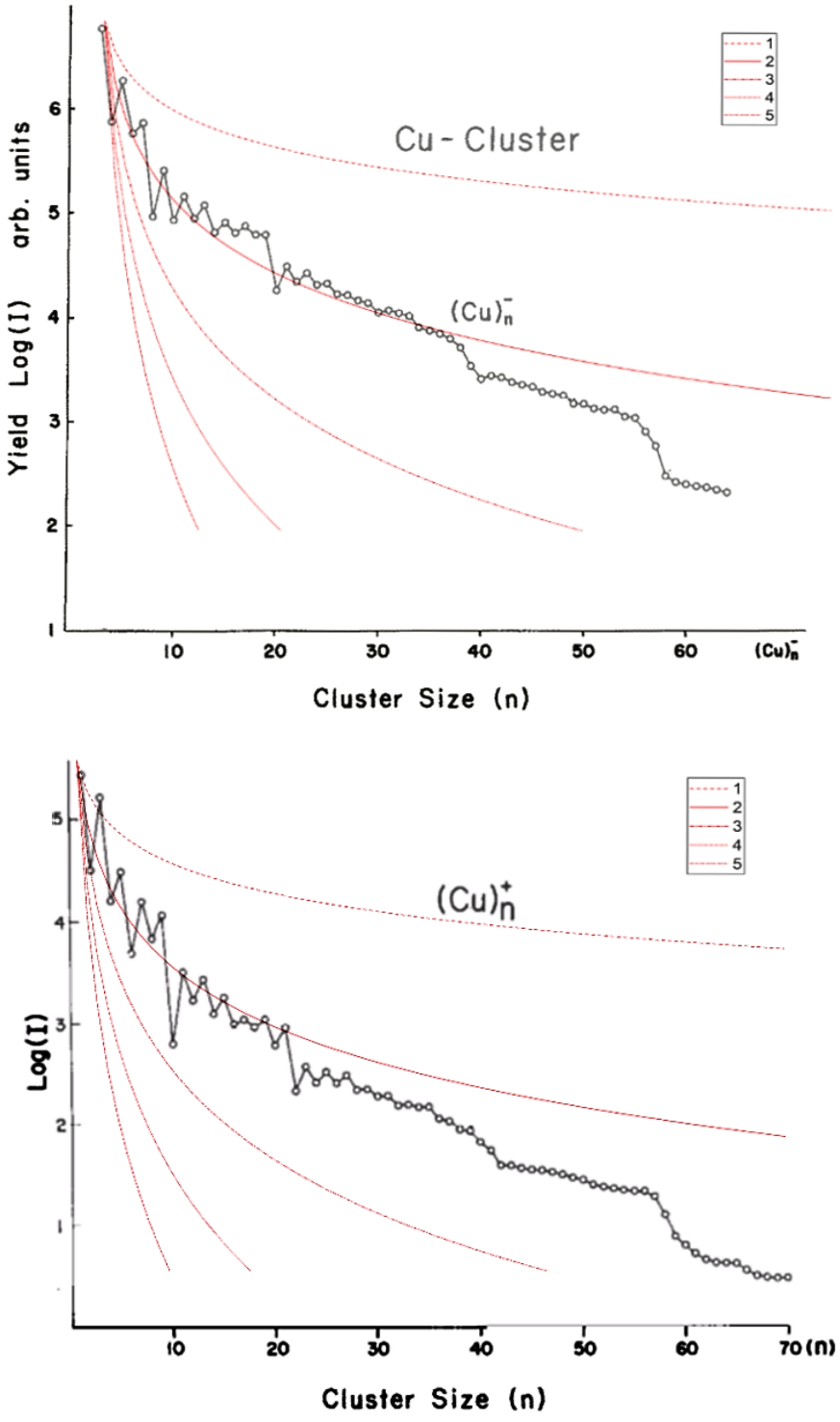

Figure 4.17: Mass spectra adapted form [27, 28]. The Red solid/dash lines are the power-law trend lines with exponent to be 1, 2, 3, 4, 5.

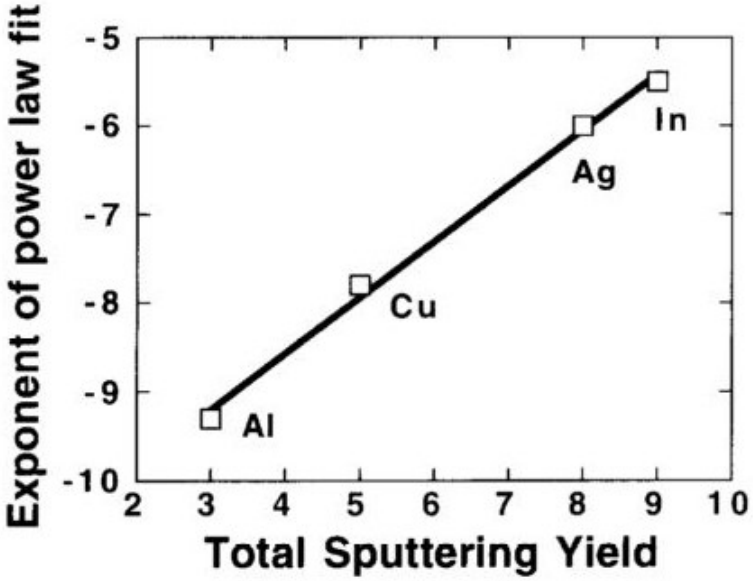

Figure 4.18: Exponent of power law fit of cluster yields versus total sputtering yield for four metals. Adapted from [13].

Chapter 5

Application of Copper Clusters

5.1 Nanoporous single-layer graphene

Clean freshwater is an essential ingredient for a healthy human life. It has been pointed out [53] that a scarcity of fresh water is a global challenge and will worsen in the future. One possible solution to this problem is desalinating seawater. With the advantages of the chemical and mechanical stability, the flexibility and one-atom thickness, the potential of using nanoporous single-layer graphene as a membrane to desalinate seawater has been proposed theoretically [9, 31] and experimentally [50]. According to recent results reported by Surwade et al., the salt rejection rate of a graphene monolayer with nanometer-sized pores can be near 100% with rapid water transport. The primary problem that needs to be solved before practical applications of graphene monolayers for water desalination is finding the best method for the fabrication of tailored nanopores of the desired dimension in suspended single-layer graphene, with high precision. One method is oxygen plasma etching that was utilized by Surwade et al.. The nanoporous single-layer graphene they tested were produced by exposure the graphene to oxygen plasma. However, oxygen plasma etching has some disadvantage. First, the density and the size of the pores both dependent on time. it was difficult to control the properties of the pores only by prolonging oxygen

plasma etching time or by adjusting the plasma density. Second, the exposure time was short for plasma-etch(0.5s to 6s) for the range of required pore sizes, which makes fine tuning hard. In other words, it is difficult to use oxygen plasma etching to produce closely and finely perforated graphene membranes.

An alternative method could be ion beam etching. Ion beam etching or milling has been sued structure metals or other materials which are not accessible to chemical etch processes. Comparing with plasma etching, ion beams have the advantage of better controllability since the size, the density and the energy of the bombardment ion beam are all selectable. Cluster ion beams offer additional advantages that the ion species, e.g., cluster sizes, can be easily selected. The feasibility of production of porous graphene by cluster ion beam bombardment is investigated, in collaboration with Dr. Ivan V. Vlassiouk of Materials Science and Technology Division at ORNL. We bombarded single-layer graphene with high energy (up to 200 keV) copper cluster ions produced with the cesium sputtering negative source

5.2 Graphene samples

The graphene samples are single-layer graphene which are synthesized using ambient pressure chemical vapor deposition (CVD) on a copper foil catalyst. They are subsequently transferred onto a silicon nitride substrate. The substrate is a circular disk of 3 mm in diameter and 0.1 mm thick. In the center of the disk is a square grid of 50 $\times$ 50 um. The mono-layer graphene is suspended over the grid. (Figure 5.1) These graphene samples were provided by Dr. Vlassiouk.

The graphene samples are small and very fragile. A special stainless steel sample holder is designed. As shown in Figure 5.2 and 5.3 , a sample is sandwiched between two stainless steel plates. The top plate has a hole of 1.27 mm (0.05") in diameter which is smaller than the sample disk but larger than the center grid for the graphene layer.The bottom plate has a 3.05 mm (0.12") in diameter groove of a depth of 0.102 mm (0.004") and a center hole of 1.27 mm (0.05") in diameter. The depth is slightly

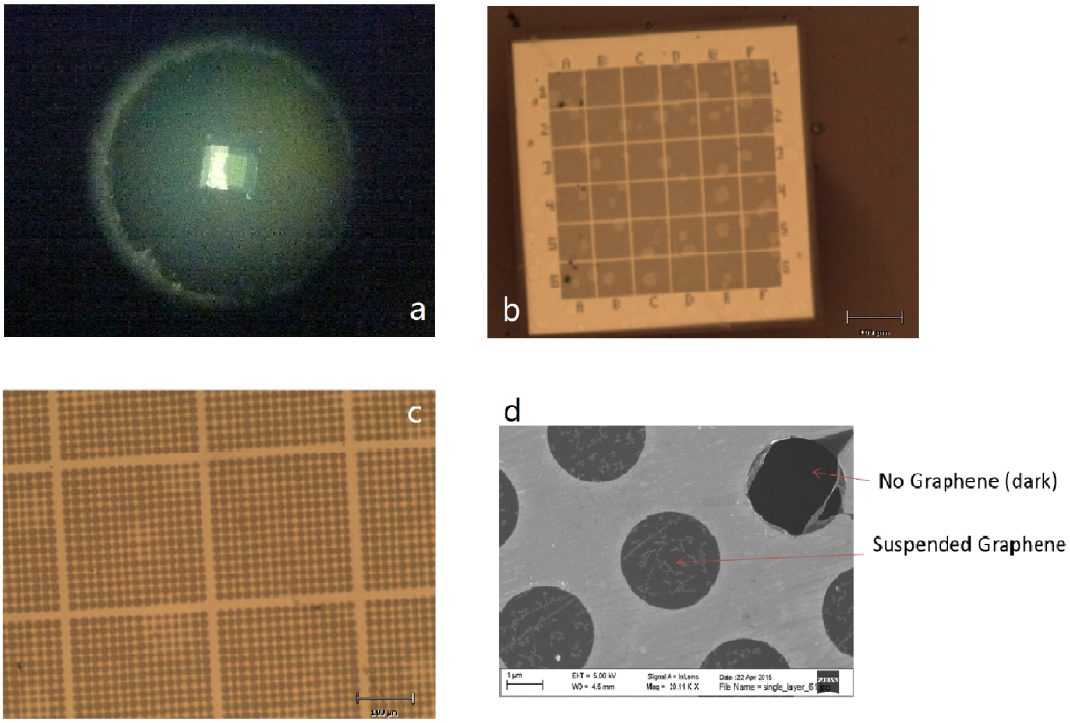

Figure 5.1: Some pictures of graphene samples. The left top is took under an optical magnifying lens. The rest are SEM/optical images. They are suspended graphene after the anneal. Some polymer residues are seen as well (in the last images).

larger than the thickness of the sample so that there is little pressure on the sample when assembled. Since the ion bombardment is conducted under vacuum, changing samples will require to bring the beamline to air and then pump down again after loading new samples. This process typically takes about one day. It is therefore desired to test multiple samples at one time. Limited by the beamline dimensions, the sample hold is deigned to have six sample grooves and up to five samples. The first sample position is left empty for ion beam intensity calibration.

5.3 Ion bombardment

The sample holder is mounted to a precision, linear motion vacuum feedthrough that is manually moved to desired sample positions. The samples are inserted into

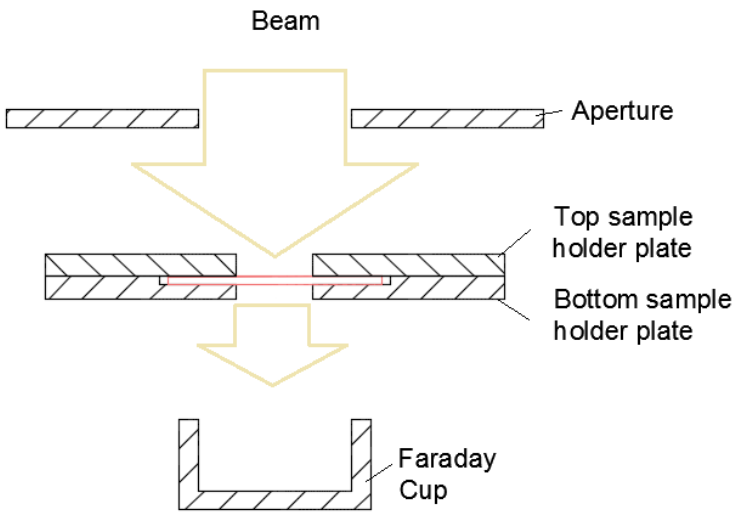

Figure 5.2: A schematic drawing of the sample holding support. It shows lateral view of the holder. The red part represents the graphene sample.

the beam line at a position after the mass analyzer magnet and before Faraday cup detector. (Shown in Figure 5.4). To avoid ion beam hitting more than one samples at one time, an aperture plate with a 3.175 mm (0.125") in diameter aperture is added in front of the sample holder, as shown in Figure 5.2 . The aperture plate is fixed, while the sample holder can be moved horizontally in and out of the beam.

The ion bombardment time depends on the desired irradiation dosages D and the ion beam intensity I. Assuming the ion beam is uniformly distributed across the graphene sample, which is generally true since the ion beam size is typically 2-3 mm in diameter, much larger than the graphene sample ($50 \times 50\ \mu m$), the bombardment time t (seconds) is given by

$$t = \frac{qAD}{I}, \tag{5.1}$$

where I is the ion intensity irradiated on the sample, and D is the desired dosage (number of ions per square centimeter), $A = \pi \times (\frac{0.127}{2})^2$ cm^2 $= 0.0127$ cm^2 is the cross section of the irradiating beam (the area of the holes on the top plate) and $q = 1.6 \times 10^{-19}$C is the charge of an electron (copper cluster ion). During the

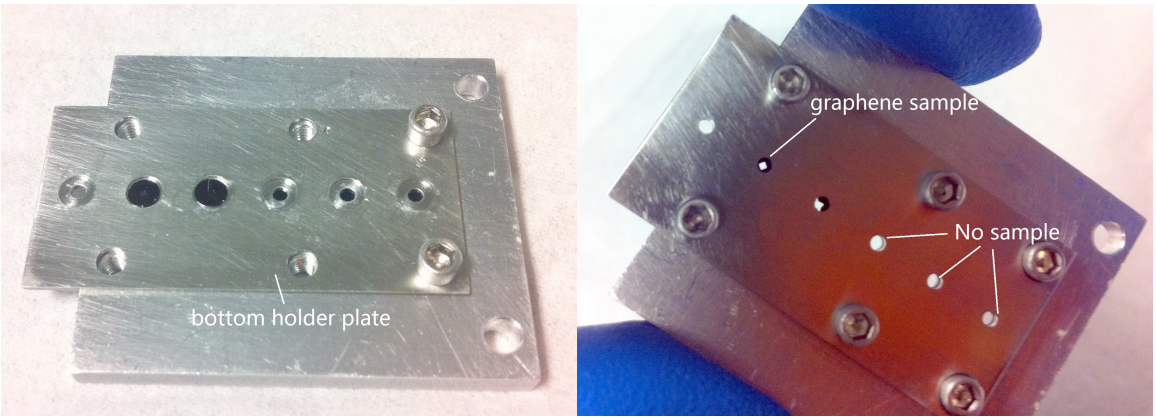

(a) **(b)**

Figure 5.3: Photograph of sample holder. (a) shows the bottom plate with grooves. (b) shows sandwiched samples with first, fourth, fifth and sixth hole empty, second hole holds a good sample and the third hole holds a broken sample.

experiment, first empty sample position is first placed into the ion beam. The ion beam intensity passing through the sample holder and measured by the down-stream Faraday cup is used to calculate the exposure time using Equation 5.1.

Three bombardment experiments have been conducted. Each experiment used five samples and five dosages:

1. Bombardment with Cu cluster size n = 9 at 200 keV ion energy and dosages of 1×10^{11}, 5×10^{11}, 1×10^{12}, 5×10^{12}, 1×10^{13} ions per square centimeter.

2. Bombardment with Cu cluster size n = 3 at 200 keV ion energy and dosages of 1×10^{11}, 3×10^{11}, 1×10^{12}, 3×10^{12}, 1×10^{13} ions per square centimeter.

3. Bombardment with Cu cluster size n = 9 at 200 keV ion energy and the same dosages as that of n = 3 clusters.

For the first experiment, the intensity of Cu_9^- measured after the empty sample whole was 0.01 nA. The corresponding bombardment times for the five dosages are given in Table 5.1. For the second and third experiments, the ion intensity was controlled to 0.04 nA so that the bombardment times were shorter. The dosages and bombardment times used for the 2nd and 3rd experiments are also given in Table 5.1. During all the experiments, the ion intensity was measured before and

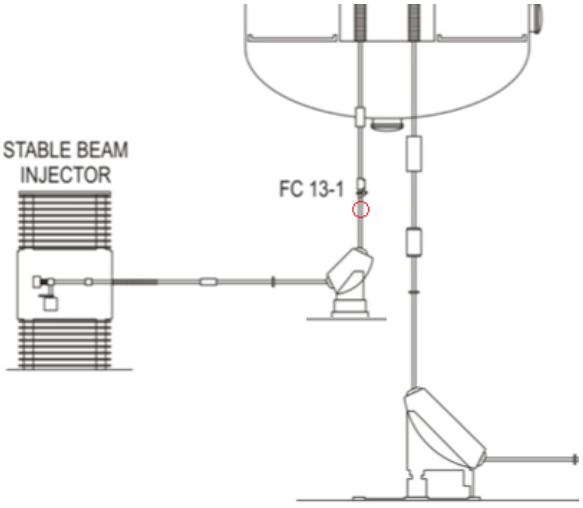

Figure 5.4: Sample position. Marked with red circle. FC13-1 is the Faraday cup we used to do mass scan which we discussed in Chapter 4.

Table 5.1: Exposure time of graphene bombardment experiment.

Label	1st run (0.01 nA)		2nd run(0.01nA)		3rd run(0.017 nA)	
	D (cm^{-2})	t (s)	D (cm^{-2})	t (s)	D (cm^{-2})	t (s)
1	1e11	20.3	1e11	20.3	1e11	11.9
2	5e11	102	3e11	61	3e11	36
3	1e12	203	1e12	203	1e12	120
4	5e12	1015	3e12	609	3e12	358
5	1e13	2026	1e13	2026	1e13	1194

after bombardment and was found to be almost constant throughout the entire experiments.

One advantage we should emphasize is that the ion intensity can be well controlled. It can be decreased to give a more accurate exposure time control for low dosages or increased for more reasonable exposure times at high dosages.

5.4 Results and discussion

After bombardment with the Cu cluster ion beams, the graphene samples were evaluated using Raman spectroscopy and scanning electron microscopy (SEM) and

the result is promising. Figure 5.5 and 5.6c shows the SEM image and the Raman spectra of the graphene samples used in the first experiment bombarded with $n = 9$ Cu cluster beams. Figure 5.6a, 5.6cand 5.6d compares the Raman spectra with (upper curve) and without (lower curve) ion bombardment. The bombarded graphene exhibits three peaks at wavelengths of 1350 cm^{-1}, 1580 cm^{-1}, and 2700 cm^{-1}, while the non-bombarded graphene has only two peaks. The extra peak at 1350 cm^{-1} isthe characteristic disorder peak D that indicates the presence of defects or pores in the graphene. The intensity of this peak also increases with irradiation dosage. It increased as it should be since I_D/I_G measures defects. Therefore, Raman spectrum showed high intensity defects appeared after ion bombardment. Figure 5.5 is the SEM image of the bombarded graphene sample , the defects of first copper cluster $n = 9$ bombardment are 2 nm pores. A appropriate size for desalinating seawater is 0.2 nm. Considering the size and the energy of the injecting copper cluster can be well controlled, we can draw from our current results is that its possible to control the size and the density of the defects on graphene in our copper cluster etching method, and hence the application is possible.

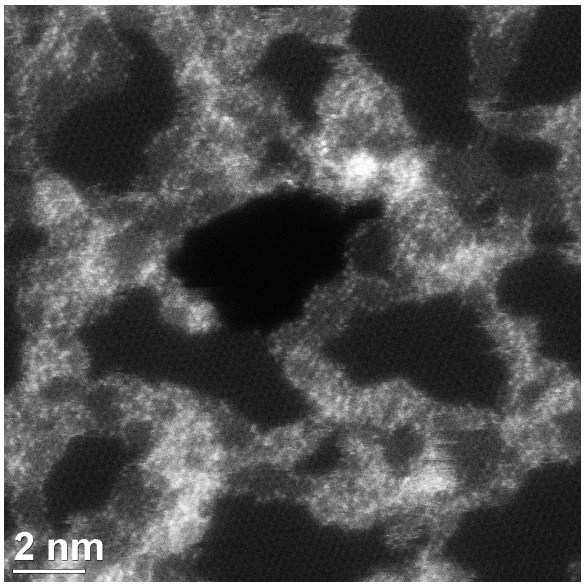

Figure 5.5: SEM image of bombarded samples.

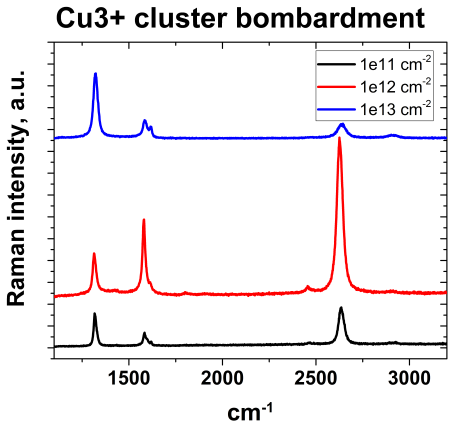

(a)

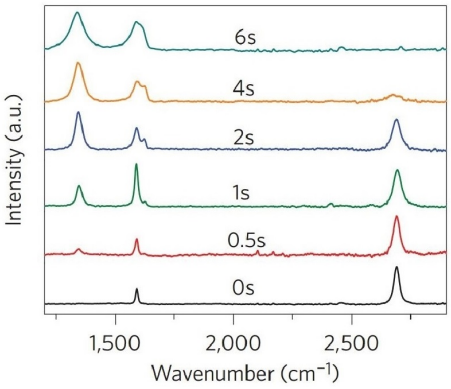

(b) Raman spectra of plasma-etching. Adapted from [50]

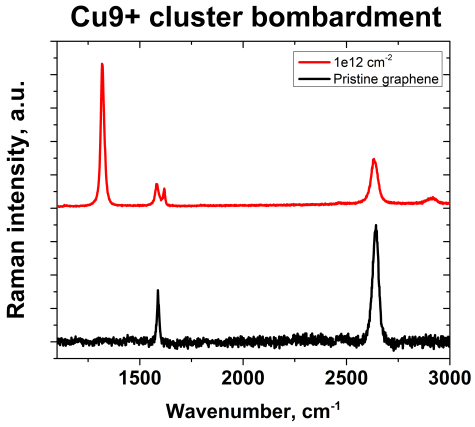

(c)

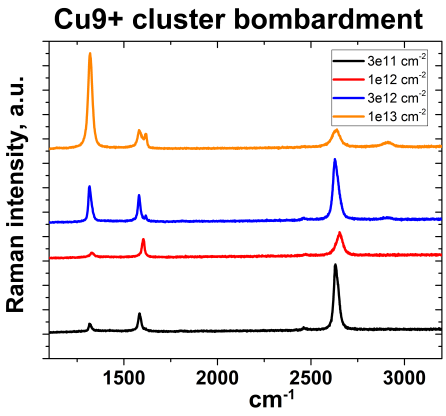

(d)

Figure 5.6: Raman spectra of bombarded samples. The unbombarded graphene is observed to exhibit a strong G peak at 1580 cm^{-1} and 2D peak at 2700 cm^{-1}. And the 2D peak is approximately three times stronger than the G peak. Bombarded samples.

Chapter 6

Conclusions

Mass distribution of copper $(Cu)_n^-$ clusters were investigated up to cluster size $n = 54$. The clusters were produced by sputtering Cs ion source with energy 1 keV to 8 keV on nature copper targets, clean copper targets, enriched copper 63 targets and enriched copper 65 targets and were analyzed using the magnetic mass analyzer. Its the first time for observe sputter Cs source produced negative copper cluster size up to 54. The mass distribution for these negative copper cluster was similar: even-odd alternated, where the intensity of odd-n cluster was greater than that of even-n, magic number existed, where the intensity decreasing discontinuously, and the ion intensity of clusters decreased with increasing cluster size n, following a power law. Its for the first time to report experimental power-law exponent of copper cluster low to 3.

The binomial distribution was observed for the first time in nature copper target mass spectra and clean copper target mass spectra. Binomial distribution indicates the sputtered copper clusters were formed after being sputtered.

The application of copper clusters we explored is utilizing the energy-and-mass-selected copper cluster to prepare nanoporous graphene for applications such as water desalination. Copper clusters of size ($n = 3$ and 9) and energy 200 keV were applied to bombard the single-layer graphene with various dosages. The Raman spectrum showed increasing defects on the graphene with increasing irradiation and 2nm size

holes were created with copper clusters of size $n = 9$ shown by SEM image. This promising results indicates the potential of the use of clusters for applications.

Bibliography

[1] S. Belykh, V. Palitsin, I. Veryovkin, A. Adriaens, and F. Adams. Non-additive sputtering of niobium and tantalum as neutral and charged clusters. *Nuclear Instruments and Methods in Physics Research Section B: Beam Interactions with Materials and Atoms*, 203:164–171, Apr 2003. ISSN 0168583X. doi: 10.1016/S0168-583X(02)02212-7. URL http://linkinghub.elsevier.com/retrieve/pii/S0168583X02022127. 13

[2] A. Benninghoven. Surface investigation of solids by the statical method of secondary ion mass spectroscopy (SIMS). *Surface Science*, 35:427–457, Mar 1973. ISSN 00396028. doi: 10.1016/0039-6028(73)90232-X. URL http://linkinghub.elsevier.com/retrieve/pii/003960287390232X. 11

[3] A. Benninghoven. Developments in secondary ion mass spectroscopy and applications to surface studies. *Surface Science*, 53(1):596–625, Dec 1975. ISSN 00396028. doi: 10.1016/0039-6028(75)90158-2. URL http://linkinghub.elsevier.com/retrieve/pii/0039602875901582. 6

[4] G. Betz and W. Husinsky. Modelling of cluster emission from metal surfaces under ion impact. *Philosophical transactions. Series A, Mathematical, physical, and engineering sciences*, 362(1814):177–94, 2004. ISSN 1364-503X. doi: 10.1098/rsta.2003.1302. URL http://www.ncbi.nlm.nih.gov/pubmed/15306283. 52

[5] I. Bitensky and E. Parilis. Shock wave mechanism for cluster emission and organic molecule desorption under heavy ion bombardment. *Nuclear Instruments and Methods in Physics Research Section B: Beam Interactions with*

Materials and Atoms, 21(1-4):26–36, Jan 1987. ISSN 0168583X. doi: 10.1016/0168-583X(87)90135-2. URL http://linkinghub.elsevier.com/retrieve/pii/0168583X87901352. 12, 13, 52

[6] M. Brack. The physics of simple metal clusters: self-consistent jellium model and semiclassical approaches. *Reviews of modern physics*, 65(677), 1993. doi: 10.1103/RevModPhys.65.677. 2

[7] O. Cheshnovsky, K. Taylor, J. Conceicao, and R. E. Smalley. Ultraviolet Photoelectron Spectra of Mass Selected Copper Clusters: Evolution of the 3d Band. *Physical review letters*, 64(15):1785–1788, 1990. ISSN 0031-9007. doi: 10.1103/PhysRevLett.64.1785. 4

[8] O. B. Christensen. Energetics and structure of negatively charged cu clusters. *PHYSICAL REVIEW B*, 50(1844), 1994. doi: 10.1103/PhysRevB.50.1844. 35

[9] D. Cohen-Tanugi and J. C. Grossman. Water Desalination across Nanoporous Graphene. *Nano Letters*, 12(7):3602–3608, Jul 2012. ISSN 1530-6984. doi: 10.1021/nl3012853. URL http://pubs.acs.org/doi/abs/10.1021/nl3012853. 55

[10] T. J. Colla and H. M. Urbassek. Effect of energy density on cluster formation from energized metals. *Computational Materials Science*, 6(1):7–14, 1996. ISSN 09270256. doi: 10.1016/0927-0256(94)00006-9. 11, 13

[11] T. J. Colla, H. Urbassek, A. Wucher, C. Staudt, R. Heinrich, B. Garrison, C. Dandachi, and G. Betz. Experiment and simulation of cluster emission from 5 KeV Ar to Cu. *Nuclear Instruments and Methods in Physics Research Section B: Beam Interactions with Materials and Atoms*, 143(3):284–297, 1998. 51, 52

[12] S. Coon, W. Calaway, M. Pellin, and J. White. New findings on the sputtering of neutral metal clusters. *Surface Science*, 298(1):161–172, 1993. ISSN 00396028.

doi: 10.1016/0039-6028(93)90092-X. URL http://linkinghub.elsevier.com/retrieve/pii/003960289390092X. 12, 13, 51

[13] S. Coon, W. Calaway, and M. Pellin. Neutral copper cluster sputtering yields: Ne+ Ar+ and Xe+ bombardment. *Nuclear Instruments and Methods in Physics Research Section B: Beam Interactions with Materials and Atoms*, 90(1-4):518–522, May 1994. ISSN 0168583X. doi: 10.1016/0168-583X(94)95606-5. 12, 13, 44, 51, 52, 54

[14] S. R. Coon, W. F. Calaway, J. W. Burnett, M. J. Pellin, and D. M. Gruen. Yields and kinetic energy distributions copper clusters of sputtered neutral. 259: 275–287, 1991. 4, 12

[15] W. A. de Heer. The physics of simple metal clusters: experimental aspects and simple models. *Reviews of Modern Physics*, 65(3):611–676, 1993. ISSN 0034-6861. doi: 10.1103/RevModPhys.65.611. URL http://link.aps.org/doi/10.1103/RevModPhys.65.611. 4

[16] S. G. Frauendorf and C. Guet. Atomic Clusters as A Branch of Nuclear Physics. *Annual Review of Nuclear and Particle Science*, 51(1):219–259, Dec. 2001. ISSN 0163-8998. doi: 10.1146/annurev.nucl.51.101701.132354. URL http://www.annualreviews.org/doi/abs/10.1146/annurev.nucl.51.101701.132354. 1

[17] R. B. Freas and J. E. Campana. Reactions of sputtered copper cluster ions. *Journal of the American Chemical Society*, 107(22):6202–6204, Oct 1985. ISSN 0002-7863. doi: 10.1021/ja00308a010. URL http://pubs.acs.org/doi/abs/10.1021/ja00308a010. 4

[18] W. Gerhard and H. Oechsner. Mass spectrometry of neutral molecules sputtered from polycrystalline metals by Ar^+-ions of 100-1000 eV. *Zeitschrift fr Physik B Condensed Matter and Quanta*, 22(1):41–48, Mar 1975. ISSN 0340-224X. doi: 10.

1007/BF01325458. URL http://link.springer.com/10.1007/BF01325458. 11

[19] S. Ghalab. *Metal cluster sputtering under reactive ion bombardment investigated by TOF-SNMS-laser-system*. PhD thesis, 2005. 8, 9, 11, 33

[20] O. F. Hagena. Cluster ion sources (invited). *Review of Scientific Instruments*, 63(4):2374–2379, 1992. ISSN 00346748. doi: 10.1063/1.1142933. 4

[21] W. M. Haynes. *CRC handbook of chemistry and physics*. CRC press, 2014. 15

[22] R. Hellborg and G. Skog. Accelerator mass spectrometry. *Mass Spectrometry Reviews*, 27(5):398427, 2008. doi: 10.1002/mas.20172. 16

[23] R. F. K. Herzog, W. P. Poschenrieder, and F. G. Satkiewicz. Observation of clusters in a sputtering ion source. *Radiation Effects*, 18(3-4):199–205, 1973. ISSN 0033-7579. doi: 10.1080/00337577308232122. 6

[24] M. S. Janzen. Testing a novel technique to improve aluminum-26 accelerator mass spectrometry measurements for earth science applications. 2012. 21

[25] M. Kabir, A. Mookerjee, and A. K. Bhattacharya. Structure and stability of copper clusters : A tight-binding molecular dynamics study. (Ci), Oct 2003. doi: 10.1103/PhysRevA.69.043203. URL http://arxiv.org/abs/physics/0310144http://dx.doi.org/10.1103/PhysRevA.69.043203. 4

[26] M. M. Kappes, M. Schaer, and E. Schumacher. Are Cluster Abundances Thermodynamic Properties? Observation of Lithium Enrichment in $Li_xNa_{n-x}, n \leq 42$. *The Journal of Physical Chemistry*, 91(3):658–663, Jan 1987. ISSN 0022-3654. doi: 10.1021/j100287a032. URL http://pubs.acs.org/doi/abs/10.1021/j100287a032. 39

[27] I. Katakuse, T. Ichihara, Y. Fujita, T. Matsuo, T. Sakurai, and H. Matsuda. Mass distributions of copper, silver and gold clusters and electronic shell structure.

International Journal of Mass Spectrometry and Ion Processes, 67(2):229–236, Nov 1985. ISSN 01681176. doi: 10.1016/0168-1176(85)80021-5. URL http://linkinghub.elsevier.com/retrieve/pii/0168117685800215. 4, 35, 51, 52, 53

[28] I. Katakuse, T. Ichihara, Y. Fujita, T. Matsuo, T. Sakurai, and H. Matsuda. Mass distributions of negative cluster ions of copper, silver, and gold. *International Journal of Mass Spectrometry and Ion Processes*, 74:33–41, 1986. doi: 10.1016/0168-1176(86)85021-2. 4, 33, 34, 37, 38, 53

[29] B. King, J. Moore, A. Zinoviev, I. Veryovkin, and M. Pellin. Sputtering of clusters from copper gold alloys. *Nuclear Instruments and Methods in Physics Research Section B: Beam Interactions with Materials and Atoms*, 267(16):2757–2760, aug 2009. ISSN 0168583X. doi: 10.1016/j.nimb.2009.05.067. URL http://linkinghub.elsevier.com/retrieve/pii/S0168583X09006405. 12, 13, 39, 51

[30] M. E. Kishinevskii. Secondary negative-ion emission. *Zhurnal Tekhnicheskoi Fiziki*, 48:773–779, 1978. 15, 19

[31] D. Konatham, J. Yu, T. A. Ho, and A. Striolo. Simulation Insights for Graphene-Based Water Desalination Membranes. *Langmuir*, 29(38):11884–11897, Sep 2013. ISSN 0743-7463. doi: 10.1021/la4018695. URL http://pubs.acs.org/doi/abs/10.1021/la4018695. 55

[32] V. E. Krohn. Emission of Negative Ions from Metal Surfaces Bombarded by Positive Cesium Ions. *Journal of Applied Physics*, 33(12):3523, 1962. ISSN 00218979. doi: 10.1063/1.1702439. URL http://scitation.aip.org/content/aip/journal/jap/33/12/10.1063/1.1702439. 6, 14, 15

[33] C. Lechene, F. Hillion, G. McMahon, D. Benson, A. M. Kleinfeld, J. P. Kampf, D. Distel, Y. Luyten, J. Bonventre, D. Hentschel, K. Park, S. Ito,

M. Schwartz, G. Benichou, and G. Slodzian. High-resolution quantitative imaging of mammalian and bacterial cells using stable isotope mass spectrometry. *Journal of Biology*, 5(6):20, 2006. ISSN 14754924. doi: 10.1186/jbiol42. URL http://jbiol.biomedcentral.com/articles/10.1186/jbiol42. 7

[34] D. G. Leopold, J. Ho, and W. C. Lineberger. Photoelectron spectroscopy of mass-selected metal cluster anions. I. Cun, n=110. *The Journal of Chemical Physics*, 86(4):1715, 1987. ISSN 00219606. doi: 10.1063/1.452170. URL http://scitation.aip.org/content/aip/journal/jcp/86/4/10.1063/1.452170. 4

[35] Z. Ma. Sputtering of neutral and ionic indium clusters. *Journal of Vacuum Science & Technology A: Vacuum, Surfaces, and Films*, 12(4):2425, Jul 1994. ISSN 07342101. doi: 10.1116/1.579185. 13

[36] K. Meiwes-Broer. Electronic properties of free and supported metal clusters studied by photoelectron spectroscopy. *Applied Physics A: Materials Science \& Processing*, 55:430–441, 1992. URL http://www.springerlink.com/index/M754030N14333335.pdf. 4

[37] S. C. O'Brien, Y. Liu, Q. Zhang, J. R. Heath, F. K. Tittel, R. F. Curl, and R. E. Smalley. Supersonic cluster beams of IIIV semiconductors: GaxAsy. *The Journal of Chemical Physics*, 84(7):4074, 1986. ISSN 00219606. doi: 10.1063/1.450069. URL http://scitation.aip.org/content/aip/journal/jcp/84/7/10.1063/1.450069. 39

[38] D. Palioselitis. Results on neutrinoless double beta decay of ^{76}Ge from Gerda Phase I. *Journal of Physics: Conference Series*, 606(012006), 2015. doi: 10.1088/1742-6596/606/1/012006,. 3

[39] C. L. Pettiette, S. H. Yang, M. J. Craycraft, J. Conceicao, R. T. Laaksonen, O. Cheshnovsky, and R. E. Smalley. Ultraviolet photoelectron spectroscopy of copper clusters. *The Journal of Chemical Physics*, 88(9):5377, 1988. ISSN

00219606. doi: 10.1063/1.454575. URL http://scitation.aip.org/content/aip/journal/jcp/88/9/10.1063/1.454575. 4, 15

[40] D. Phillips II, E. Aguayo, F. Avignone III, H. O. Back, A. S. Barabash, M. Bergevin, F. Bertrand, M. Boswell, V. Brudanin, M. Busch, et al. The majorana experiment: an ultra-low background search for neutrinoless double-beta decay. In *Journal of Physics: Conference Series*, volume 381, page 012044. IOP Publishing, 2012. 3

[41] L. E. Rehn, R. C. Birtcher, S. E. Donnelly, P. M. Baldo, and L. Funk. Origin of Atomic Clusters during Ion Sputtering. *Physical Review Letters*, 87(20):207601, Oct 2001. ISSN 0031-9007. doi: 10.1103/PhysRevLett.87.207601. URL http://link.aps.org/doi/10.1103/PhysRevLett.87.207601. 12

[42] E. Romero-Romero. Ph.D Thesis . *University of Tennessee*, in progress. 4

[43] M. Sakurai, K. Watanabe, K. Sumiyama, and K. Suzuki. Magic numbers in transition metal (Fe, Ti, Zr, Nb, and Ta) clusters observed by time-of-flight mass spectrometry. *The Journal of Chemical Physics*, 111:235–238, 1999. ISSN 00219606. doi: 10.1063/1.479268. URL http://link.aip.org/link/?JCP/111/235/1. 4

[44] G. Schmid and D. Fenske. Metal clusters and nanoparticles. *The Royal Society*, 368, 2010. doi: 10.1098/rsta.2009.0281. 2

[45] P. Sigmund. Theory of Sputtering. I. Sputtering Yield of Amorphous and Polycrystalline Targets. *Physical Review*, 184(2):383–416, aug 1969. ISSN 0031-899X. doi: 10.1103/PhysRev.184.383. URL http://link.aps.org/doi/10.1103/PhysRev.184.383. 8, 9

[46] P. Sigmund. A mechanism of surface micro-roughening by ion bombardment. *Journal of Materials Science*, 8(11):1545–1553, 1973. ISSN 00222461. doi: 10.1007/BF00754888. 7, 9, 10

[47] P. Sigmund. Energy density and time constant of heavy-ion-induced elastic-collision spikes in solids. *Applied Physics Letters*, 25(3):169, 1974. ISSN 00036951. doi: 10.1063/1.1655425. URL http://scitation.aip.org/content/aip/journal/apl/25/3/10.1063/1.1655425. 12

[48] P. Sigmund. Sputtering from elastic-collision spikes in heavy-ion-bombarded metals. *Journal of Applied Physics*, 52(2):990, 1981. ISSN 00218979. doi: 10.1063/1.328790. URL http://scitation.aip.org/content/aip/journal/jap/52/2/10.1063/1.328790. 8

[49] C. Staudt and A. Wucher. Generation of large indium clusters by sputtering. *Physical Review B*, 66(7):075419, aug 2002. ISSN 0163-1829. doi: 10.1103/PhysRevB.66.075419. URL http://link.aps.org/doi/10.1103/PhysRevB.66.075419. 12, 13

[50] S. P. Surwade, S. N. Smirnov, I. V. Vlassiouk, R. R. Unocic, G. M. Veith, S. Dai, and S. M. Mahurin. Water desalination using nanoporous single-layer graphene. *Nature Nanotechnology*, 10:459–464, 2015. doi: 10.1038/nnano.2015.37. 55, 62

[51] C. Tuniz, W. Kutschera, D. Fink, G. F. Herzog, and J. R. Bird. *Accelerator mass spectrometry: ultrasensitive analysis for global science*. CRC press, 1998. 4, 16

[52] H. M. Urbassek. Sputtered cluster mass distributions, thermodynamic equilibrium and critical phenomena. *Nuclear Instruments and Methods in Physics Research Section B: Beam Interactions with Materials and Atoms*, 31(4):541–550, Jun 1988. ISSN 0168583X. doi: 10.1016/0168-583X(88)90453-3. URL http://linkinghub.elsevier.com/retrieve/pii/0168583X88904533. 11, 13, 52

[53] C. J. Vorosmarty. Global Water Resources: Vulnerability from Climate Change and Population Growth. *Science*, 289(5477):284–288, Jul 2000. ISSN 00368075.

doi: 10.1126/science.289.5477.284. URL http://www.sciencemag.org/cgi/doi/10.1126/science.289.5477.284. 55

[54] X. Wang, X. Lu, L. Shao, J. Liu, and W. Chu. Small cluster ions from source of negative ions by cesium sputtering. *Nuclear Instruments and Methods in Physics Research Section B: Beam Interactions with Materials and Atoms*, 196(1-2):198–204, Nov 2002. ISSN 0168583X. doi: 10.1016/S0168-583X(02)01302-2. URL http://linkinghub.elsevier.com/retrieve/pii/S0168583X02013022. 27

[55] A. Wucher. The mass distribution of sputtered metal clusters ii. model calculation. *Nuclear Instruments and Methods in Physics Research B*, 83(Issues 1-2):7986, 1993. doi: 10.1016/0168-583X(93)95911-N,. 52

[56] A. Wucher and M. Wahl. The formation of clusters during ion induced sputtering of metals. *Nuclear Instruments and Methods in Physics Research Section B: Beam Interactions with Materials and Atoms*, 115(1-4):581–589, Jul 1996. ISSN 0168583X. doi: 10.1016/0168-583X(96)00153-X. URL http://linkinghub.elsevier.com/retrieve/pii/0168583X9600153X. 11, 12, 13

[57] A. Wucher, M. Wahl, and H. Oechsner. The mass distribution of sputtered metal clusters. I Experiment. *Nuclear Instruments and Methods in Physics Research*, B83:73–78, 1993. ISSN 0168583X. 4, 12, 13, 44

[58] X. Zhang, Z. Tang, and Z. Gao. Formation, growth mechanism and packing sequences of binary alloy cluster anions from laser ablation of mixtures of lead and transition metals. *Rapid Communications in Mass Spectrometry*, 17(6):621–626, Mar 2003. ISSN 0951-4198. doi: 10.1002/rcm.956. URL http://doi.wiley.com/10.1002/rcm.956. 39

[59] L. Zheng, C. M. Karner, P. J. Brucat, S. H. Yang, C. L. Pettiette, M. J. Craycraft, and R. E. Smalley. Photodetachment studies of metal clusters: Electron affinity

measurements for cu_x. *The Journal of Chemical Physics*, 85(1681), 1986. doi: 10.1063/1.451838. 4

Vita

Ran Chu was born and raised in China. She received her B.A. in physics from South China University of Technology in 2013. Since 2013, she moved to Knoxville, TN. Most of her "spare time" was spent in gardening and stargazing. Dream to know, and understand if possible, this world.